Acta Oceanol. Sin., 2022, Vol. 41, No. 10, P. 54–73
https://doi.org/10.1007/s13131-022-2017-1
http://www.aosocean.com
E-mail: ocean2@hyxb.org.cn

Variations of suspended sediment transport caused by changes in shoreline and bathymetry in the Zhujiang (Pearl) River Estuary in the wet season

Shicheng Lin[1, 2, 3], Jianwei Niu[1, 2, 3]*, Guangping Liu[1, 2], Xing Wei[1, 2, 4], Shuqun Cai[1, 2, 4]*

[1] State Key Laboratory of Tropical Oceanography, South China Sea Institute of Oceanology, Chinese Academy of Sciences, Guangzhou 510301, China

[2] Southern Marine Science and Engineering Guangdong Laboratory (Guangzhou), Guangzhou 511458, China

[3] University of Chinese Academy of Sciences, Beijing 100049, China

[4] Institution of South China Sea Ecology and Environmental Engineering, Chinese Academy of Sciences, Guangzhou 510301, China

Received 6 January 2022; accepted 14 March 2022

Abstract

A wave-current-sediment coupled numerical model is employed to study the responses of suspended sediment transport in the wet season to changes in shoreline and bathymetry in the Zhujiang (Pearl) River Estuary (ZRE) from 1971 to 2012. It is shown that, during the wavy period, the large wave-induced bottom stress enhances sediment resuspension, resulting in an increase in the area of suspended sediment concentration (SSC) greater than 100 mg/L by 183.4%. On one hand, in spring tide, the change in shoreline reduces the area of SSC greater than 100 mg/L by 17.8% in the west shoal (WS) but increases the SSC, owing to the closer sediment source to the offshore and the stronger residual current at the Hengmeng (HEM) and Hongqili (HQL) outlets. The eastward Eulerian transport is enhanced in the WS and west channel (WC), resulting in a higher SSC there. The reclamation of Longxue Island (LXI) increases SSC on its east side and east shoal (ES) but decreases the SSC on its west and south sides. Moreover, in the WC, the estuarine turbidity maximum (ETM) is located near the saltwater wedge and moves southward, which is caused by the southward movement of the maximum longitudinal Eulerian transport. In neap tide, the changes are similar but relatively weaker. On the other hand, in spring tide, the change in bathymetry makes the SSC in the WS increase, and the area of SSC greater than 100 mg/L increases by 11.4% and expands eastward and southward, which is caused by the increases in wave-induced bottom stress and eastward Eulerian transport. On the east side of the WC, the eastward Eulerian transport decreases significantly, resulting in a smaller SSC in the middle shoal (MS). In addition, in the WC, the maximum SSC is reduced, which is caused by the smaller wave-induced bottom stress and a significant increase of 109.88% in southward Eulerian transport. The results in neap tide are similar to those in spring tide but with smaller changes, and the sediment transports northward in the WC owing to the northward Eulerian transport and vertical shear transport. This study may provide some references for marine ecological environment security and coastal management in the ZRE and other estuaries worldwide affected by strong human interventions.

Key words: suspended sediment concentration, wave, bottom stress, estuarine turbidity maximum, numerical model, Zhujiang (Pearl) River Estuary

Citation: Lin Shicheng, Niu Jianwei, Liu Guangping, Wei Xing, Cai Shuqun. 2022. Variations of suspended sediment transport caused by changes in shoreline and bathymetry in the Zhujiang (Pearl) River Estuary in the wet season. Acta Oceanologica Sinica, 41(10): 54–73, doi: 10.1007/s13131-022-2017-1

1 Introduction

Estuaries, the transitional zones between rivers and seas, have long been recognized as efficient traps for fluvial and marine sediments, leading to estuarine turbidity maxima (ETMs) with high concentrations of suspended particulate matter (SPM) (Meade, 1969; Burchard et al., 2018). The maximum suspended sediment concentration (SSC) in such ETMs typically ranges between 0.1 kg/m^3 and over 10 kg/m^3 and may be several times to orders of magnitude higher than that in the surrounding waters. Many estuaries worldwide have been modified in recent decades by human interventions, which include navigational channel dredging to support larger vessels and land reclamation to obtain more land resources. Significantly, these human interventions may greatly change estuarine hydrodynamics, thereby affecting suspended sediment transport. These changes may significantly influence the ecological functioning of the estuary

Foundation item: The National Natural Science Foundation of China under contract No. 41890851; the Key Research Program of Frontier Sciences, Chinese Academy of Sciences, under contract No. QYZDJ-SSW-DQC034; the Key Special Project for Introduced Talents Team of Southern Marine Science and Engineering Guangdong Laboratory (Guangzhou) under contract No. GML2019ZD0304; the fund of Chinese Academy of Sciences under contract No. ISEE2021PY01; the project of Department of Natural Resources of Guangdong Province under contract No. [2020]017.

*Corresponding author, E-mail: jwniu@scsio.ac.cn; caisq@scsio.ac.cn

since high SSCs are associated with a drastic reduction in oxygen levels and primary production (Cloern, 1987; Kerner, 2007; Dijkstra et al., 2019).

There are numerous studies on the responses of sediment transport to changes in the shoreline and bathymetry in many estuaries worldwide. In the North Passage of Changjiang (Yangtze) River Estuary, the dredging from 1999 to 2011 strengthened the river discharge (Dai et al., 2013). By deepening the channels in the Ems Estuary, measurements showed that the SPM in the lower reaches of the estuary had increased an average of 2- to 3-fold between 1954 and 2005, with a 10-fold increase in the upper estuary, and the ETM had moved upstream by up to 25 km (de Jonge et al., 2014; van Maren et al., 2015). Dijkstra et al. (2019) used an idealized width-averaged iFlow model to demonstrate that the increase in SSC was related to the resonance of the M_4 tide. Kerner (2007) stated that after channel deepening in 1999 in Elbe Estuary, an astonishingly small decrease of the low water level by only between 5.7 cm and 8.5 cm produced a marked increase in the retention of fine grain SPM in the freshwater, which produced an increase of the <63 mm fraction in the sediments of the Hamburg harbor by approximately 20% and in the SPM along the freshwater longitudinal profile up to ~120%. In the Seine Estuary, civil engineering works have reduced the available amount of space, leading to an increase in the natural downstream shift of the depocenter of mud brought by winter river floods (Lesourd et al., 2001). In the Ribble Estuary, the triggering factor accelerating sedimentation was embanking and reclamation, commencing in 1810, which progressively reduced the intertidal area, tidal prism and tidal current velocities within the estuary, in turn further enhancing sedimentation (van der Wal et al., 2002). In the North Branch of Changjiang River Estuary, the land reclamation strengthened the currents during flood, enhancing the channel's ability to transport sediment landward, and the variations in SSC and suspended sediment transport were also affected by couplings between fluvial runoff and tidal currents (Dai et al., 2016, 2018).

Since the reform and opening up in the 1970s, China's Zhujiang (Pearl) River Delta region has witnessed rapid economic development and frequent human interventions. Among them, coastal reclamation activities caused the shoreline of the Zhujiang River Estuary (ZRE) to continuously extend toward the sea, and the water area decreased by 244.11 km^2 from 1978 to 2014, a decrease of approximately 10%. Meanwhile, anthropogenic activities, including sand excavation and channel dredging, have caused rapid shoal siltation and channel deepening, whose effects are far beyond evolution under natural conditions (Wu et al., 2016; Yang et al., 2019). Correspondingly, the change in shoreline and bathymetry adjusted the hydrodynamics in the ZRE. Zhang et al. (2021b) found that channel deepening and narrowing in recent decades in the ZRE resulted in increasing wave celerity, amplifying tidal waves and increasing velocity amplitude. Lin et al. (2021) used a numerical model to analyze the hydrodynamics in the ZRE in 1971 and 2012, showing that the change in the shoreline increased the exchange flow by 9.5% and inhibited bottom seawater intrusion in the west channel (WC), and the change in the water depth enhanced the exchange flow by 27.5% and increased the intrusion distance of saline water in the WC by approximately 14 km.

In the ZRE, there have been a great deal of studies on suspended sediment. The distributions of different riverine sediments in the ZRE were mostly independent in neap tides but overlapped more in spring tides (Zhang et al., 2019). Sediment transport is primarily controlled by tidal currents and river discharge (Chen and Chen, 2008; Hu et al., 2011). There are different conclusions on the formation mechanism of the ETM in the ZRE. Wai et al. (2004) analyzed hydrological data from 1978 to 1979 and found that gravitational circulation, tidal trapping, and sediment resuspension and deposition processes are the primary ETM formation mechanisms in the ZRE. Shen et al. (2001) indicated that the source of sediment was fluvial sediment, and the cause of sediment enrichment was the salinity-induced density gradient. Liu et al. (2018) proposed that resuspension and gravitational circulation were the main controlling factors for the formation of the ETM, and the resuspended sediment was transported upstream to the ETM zone under the action of gravitational circulation. By using a numerical model, Yan et al. (2020) found that the main mechanism of ETM formation in the ZRE was the bottom convergence generated by residual current, and the location of the ETM was determined by horizontal advection. During dry seasons, the SSC was enhanced, and the ETM was intensified (Liu et al., 2018). The presence of waves increased the landward current and sediment transport at the bottom of the channel and the seaward fluxes of water and sediment at the west shoal (WS) and increased the lateral sediment entrapment in the southwest shoal (Zhang et al., 2021a).

Unfortunately, there are only a few studies on the mechanism of variation of suspended sediment transport with time in the ZRE. Based on the measured data of spring tides, Xie et al. (2015) showed that the orientation of net sediment transport changed from seaward in 1978 to landward after 2003, since the contribution of steady advection transport to net sediment transport was dramatically reduced, whilst Stokes drift, tidal trapping and net vertical circulation increased. Based on the underwater topographic data of ZRE since the 1970s, Yang et al. (2021) showed that the runoff channels in the west moves downward, and the sedimentation center of the WS tends to moves southward. Moreover, Zhang et al. (2021a) studied the wave effects on SSC and suspended sediment transport in the ZRE in the dry season, whilst in the wet season, few studies have deeply analyzed the wave effects.

In summary, previous studies mainly focused on the impacts of comprehensive changes in shoreline and bathymetry on suspended sediment transport in the ZRE. In fact, either change in shoreline or change in bathymetry can alter the suspended sediment transport pattern. Thus, our motivation is to separate the impacts of shoreline and bathymetry changes, i.e., what are the respective effects of the changes in shoreline and bathymetry on SSC and suspended sediment transport in the ZRE? What are the associated dynamic mechanisms? In particular, how do the wave effects vary with the changes in shoreline and bathymetry in the wet season? In this study, the main objectives focus on the above problems caused by the changes in shoreline and bathymetry of the ZRE between 1971 and 2012 by numerical simulation. The structure of the paper is as follows. Section 2 describes the model setting, validation, and methods. The model results are analyzed in Section 3, Section 4 is the discussion, and finally, the conclusions are presented in Section 5.

2 Model details

China's Zhujiang River Delta, including the ZRE, Modaomen Estuary and Huangmaohai Estuary, connects the South China Sea via eight major riverine runoff outlets, namely, Yamen, Hutiaomen, Jitimen, Modaomen, Hengmen, Hongqili, Jiaomen, and Humen (YM, HTM, JTM, MDM, HEM, HQL, JM, and HUM, respectively) (Fig. 1). The ZRE, the largest of the three estuaries, is funnel-shaped and ranges from 22°12′–22°45′N and 113°33′–114°09′E with an area of 2 110 km^2. The width at the head of the bay is about 5 km, increasing downstream to about 35 km at the mouth. The water depth in the WS, middle shoal (MS) and east

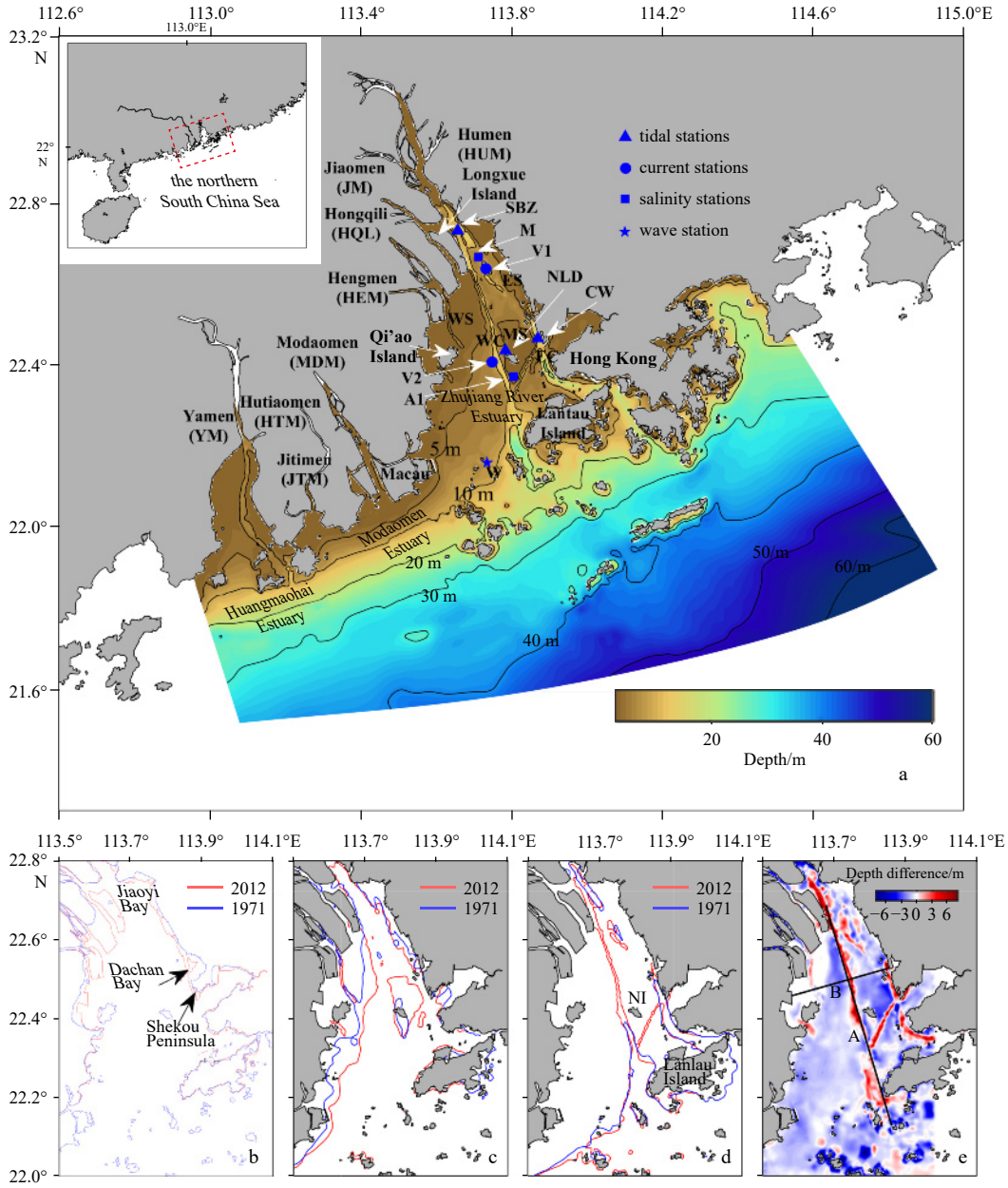

Fig. 1. Model domain, shorelines and water depth modified from Lin et al. (2021). a. Model domain (zoomed-in dashed line rectangle box in the top left corner) and bathymetry in the ZRE (shoreline and water depth are drawn from the nautical charts of 2012). WS, WC, MS, EC, and ES represent the west shoal, west channel, middle shoal, east channel and east shoal, respectively. NI represents Neilingding Island. SBZ, CW, and NLD represent Shanbanzhou, Chiwan, and Neilingding, respectively, which are tidal stations. V1 and V2 are current stations, A1 and M are salinity stations, and W is a wave station. b. Shorelines, c. 5 m isobaths and d. 10 m isobaths in the ZRE, in which the red and blue lines represent the 2012 and 1971 cases, respectively. e. Water depth difference between 2012 and 1971. Sections A and B in e are used in the following analysis.

shoal (ES) is shallower than 5 m, whereas it is nearly 5–15 m in the WC and east channel (EC) (Fig. 1).

2.1 *Model settings*

In this study, the employed coupled modeling system consists of the regional ocean modeling system (ROMS) for hydrodynamics, the community sediment transport modeling system (CSTMS) for sediment transport, and the simulating waves nearshore (SWAN) for ocean waves (Shchepetkin and McWilliams, 2005; Haidvogel et al., 2008; Booij et al., 1999). It has been widely applied in sediment transport studies (Warner et al., 2008; Zeng et al., 2015; Liu and Cai, 2019).

The model domain covers the ZRE and adjacent continental shelf waters (Fig. 1) and contains 350×340 grid cells with horizontal resolution of approximately 500 m and 16 vertical terrain-following s-levels, with high resolution near the surface and bottom to accurately resolve the surface and bottom boundary layer, with the s-grid parameters being set as θ_s=5.0 and θ_b=0.4 (Song and Haidvogel, 1994). In the ROMS model, the Mellor-Yamada 2.5 turbulence closure scheme was used to represent vertical mixing (Mellor and Yamada, 1982). The initial salinity and temperature data are extracted from the World Ocean Atlas 2009

(WOA2009), while the initial sea surface, elevation, current velocity, and SSC are set to zero. At the surface, the heat and salt fluxes are ignored, and the wind stress is calculated by the formula of Large and Pond (1981) using 10 m-high winds from National Centers for Environmental Prediction (NCEP) reanalysis data with a temporal resolution of 6 h and a spatial resolution of 0.3°×0.3° (Kalnay et al., 1996). At the bottom, the bottom-boundary layer was simulated with a formulation suitable to represent the combined effects of current, waves, and movable sediments (Styles and Glenn, 2000; Warner et al., 2008).

Nine tidal constituents (M_2, S_2, N_2, K_2, K_1, O_1, P_1, Q_1 and MS_4) derived from TPXO 7.0 are incorporated in the modeling at the east, west, and south open boundaries (Egbert and Erofeeva, 2002). At these open boundaries, the Flather and Chapman boundary conditions are applied to the barotropic current and water elevation, respectively (Chapman, 1985; Flather, 1976). Meanwhile, Orlanski radiation conditions (Orlanski, 1976) are applied for baroclinic velocities and tracers (temperature, salinity, and salinity) to minimize wave reflection from the boundaries into the inner domain.

The SWAN model has the same computational grids as the ROMS model has. The wave boundary conditions are specified by the nonstationary wave parameters from the outputs of the WAVE-WATCH III global wave model (ftp://polar.ncep.noaa.gov/pub/history/waves). Using two-way coupling applications, information (including water level, current velocity, wave elements and bottom orbital velocity) is exchanged between the ROMS and SWAN models at an interval of 1 h to introduce the wave-current interaction.

The CSTMS model is used to simulate sediment transport. Suspended sediments in the ZRE are composed of fine-grained silt and clay, with a median particle diameter of approximately 8 μm (Chen and Chen, 2008). Thus, we consider only one class of river-derived sediment for simplicity in this study, and the sediment parameter settings are listed in Table 1, following Liu and Cai (2019). The median particle diameter, settling velocity, and critical shear stress are set to 8.0 μm, 0.038 7 mm/s, and 0.022 Pa, respectively. The sediment bed is initialized with 10 vertical levels with the top 6 layers at 0.01 m thick and the bottom 4 layers at 0.10 m thick. The river sediment properties are supposed to be equivalent to the bed sediment class.

For the river discharge boundaries, the river runoff ratios at the eight outlets are prescribed according to Table 2 as provided by Yao et al. (2009), and the observed daily total river discharge flowing into the ZRE is prescribed in Fig. 2b. The volume of discharge is uniformly distributed in the water column with fluvial SSC set to 0.284 kg/m^3 (Luo et al., 2002; Hu et al., 2011; Liu and Cai, 2019). River temperature and salinity are set to 27.5℃ and 0, respectively.

Table 1. Sediment parameter settings

Parameter	Value
Diameter/μm	8.0
Settling velocity/(mm·s^{-1})	0.038 7
Critical shear stress/Pa	0.022
Density/(kg·m^{-3})	2 650
Surface erosion rate/(kg·m^{-2}·s^{-1})	0.000 002
Porosity	0.672

The shoreline and bathymetric data are obtained by interpolation of estuarine data from nautical charts (Hong Kong Maritime Department and China Maritime Safety Administration) through ArcGIS, together with the offshore data from General Bathymetric Chart of the Oceans (GEBCO; British Oceanographic Data Center) in 1971 and 2012, following Lin et al. (2021). In the model, the minimum water depth is set to 3 m, and the topography is slightly smoothed to avoid numerical instabilities in the computation. Figure 1b shows that the shoreline changes mainly occurs near HM, HQL, JM, Jiaoyi Bay and Dachan Bay in the two years. The 5 m isobath advances seaward in the WS and advances eastward and northward in the MS, and the 10 m isobath extends northward to Longxue Island (LXI) and westward to EC in 2012 compared with that in 1971 (Figs 1c and d). Moreover, WS and MS are obviously silted, ES is somewhat silted, and EC and WC are deepened significantly (Fig. 1e).

Three model cases, the 1971 case, transition case and 2012 case, are designed in this study (Table 3). The water depth and shoreline data in the 2012 (1971) case are based on the chart in 2012 (1971), while those in the transition case, the water depth is based on the chart in 1971 but the shoreline is based on the chart in 2012. The other conditions, including the initial field, boundary field and forcing conditions, are the same in the models. By comparing the 1971 case (transition case) with the transition case (2012 case), the impact of shoreline (bathymetry) change is discussed. The 2012 case is used to verify the model results and to be analyzed later. The model is run from May 1 to July 31, 2012. The first 25-day spin-up run is set to let the model adjust to the initial conditions and the various changes imposed on the scenarios.

2.2 *Model verification*

The spatial distributions of the water level, current, salinity and wave observation stations are shown in Fig. 1a, where the triangles, circles, squares, and star represent the tidal stations (CW, NLD, and SBZ), current stations (V1 and V2), salinity stations (M and A1), and wave station (W), respectively. The water elevation data were from May 1 to July 31, 2012, the current data were obtained by an acoustic Doppler current profiler from July 6 to 7, 2012, the salinity data were obtained by CTD (conductivity, temperature, depth) in June 2012, and the wave data were obtained by Waverider from June 1 to July 31, 2012.

The model validation is quantified using a skill assessment parameter (SK) (Willmott, 1981), which represents the agreement between the model and the observations, with a SK equal to one indicating perfect simulations and a value equal to zero indicating complete disagreement. The SK is defined as follows:

$$\mathrm{SK} = 1 - \frac{\sum_{i=1}^{n} \left(X_{\mathrm{mo}} - X_{\mathrm{ob}}\right)^2}{\sum_{i=1}^{n} \left(\left|X_{\mathrm{mo}} - \overline{X_{\mathrm{ob}}}\right| + \left|X_{\mathrm{ob}} - \overline{X_{\mathrm{ob}}}\right|\right)^2}, \tag{1}$$

where X_{mo}, X_{ob} and $\overline{X_{\mathrm{ob}}}$ represent the model results, the observed data, and the time-mean observed data, respectively. The Willmott skill score is widely used in the coastal ocean models (Liu et al., 2009; Liu and Cai, 2019; Zhang et al., 2021a).

Comparisons between the modeling results and *in situ* obser-

Table 2. River runoff ratios at the eight outlets

River outlet	HUM	JM	HQL	HEM	MDM	JTM	HTM	YM	Total
Ratio/%	12.1	14.0	13.2	16.2	29.6	3.7	4.9	6.3	100

Note: The eight outlets are labeled by HUM, JM, HQL, HEM, MDM, JTM, HTM, and YM, representing Humen, Jiaomen, Hongqili, Hengmen, Modaomen, Jitimen, Hutiaomen, and Yamen, respectively.

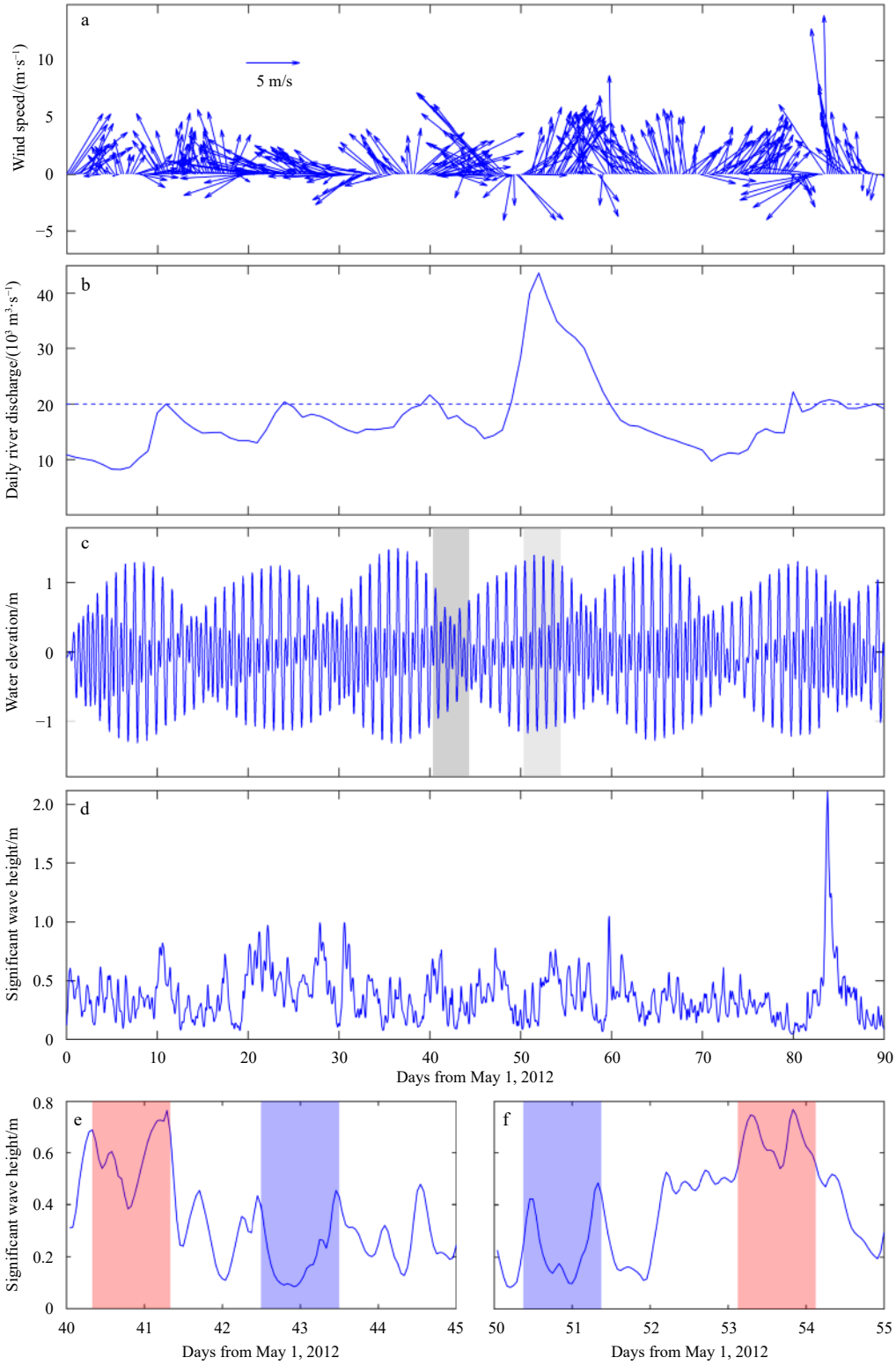

Fig. 2. Time series of wind speed at NLD (a), daily river discharge rate in the ZRE (b), water elevation at NLD (c), and significant wave height at NLD (d) from May 1, 2012, and the significant wave heights in neap (e) and spring (f) periods derived from d. The dark and light gray shadows in c are chosen as neap tide and spring tide periods, respectively, in this paper. The red and blue shadows in e and f are chosen as wavy and calm periods, respectively.

vations of the water level, current, and salinity can be found in Lin et al. (2021). Here, we only verify the significant wave height and SSC. Figure 3 shows that the simulated significant wave height coincides with the observations at the wave station with a SK value of 0.82 (Table 4), which suggests that our model reproduces the observed wave variability reasonably well. Figure 4 shows the validation of the surface and bottom SSC time series at Stas V1 and V2. The simulated SSC at Sta. V2 agrees better with

Table 3. Coastlines and bathymetries of the ZRE in the three model scenarios

Scenario	Coastline	Bathymetry
1971 case	1971	1971
Transition case	2012	1971
2012 case	2012	2012

the observed value than that at Sta. V1, and their SK values are 0.77 and 0.56 (Table 4), respectively.

The SSC data in the ZRE (Zhan et al., 2019) derived from the moderate resolution imaging spectroradiometer MODIS Level-1B data at 1 km resolution are used here to validate the simulated spatial distribution of surface SSC in the ZRE. The comparison results generally illustrate a fairly consistent spatial distribution of suspended sediments in the surface layer of the ZRE (Fig. 5).

In conclusion, the validations of the temporal and spatial distributions of SSC indicated that the model is reliable for the analysis of sediment dynamics in the ZRE.

2.3 *Methods*

In this paper, the north (south) of the NI is defined as the upstream (downstream) of the ZRE (Fig. 1e), and the neap tide and spring tide periods are defined by dark and light gray shadows in Fig. 2c, respectively. The residual current is defined as the tidally averaged velocity in neap or spring tide periods, and the surface (bottom) layer represents the top-most (bottom-most) layer.

Referring to the method of mass transport flux suggested by Dyer (1974), velocity u and sediment concentration c at any depth can be written as

$$\begin{cases} u = \overline{u} + u_v \\ c = \overline{c} + c_v \\ \overline{u} = \dfrac{1}{h}\displaystyle\int_0^h u \cdot \mathrm{d}z \\ \overline{c} = \dfrac{1}{h}\displaystyle\int_0^h c \cdot \mathrm{d}z \end{cases}, \tag{2}$$

where u_v and c_v are the deviations at any depth from the mean values $\overline{u}$ and $\overline{c}$, h is the water depth and z is the vertical coordinate. u and c will vary over tidal cycles due to tidal fluctuations. Thus, u and c can be expressed by the sum of the tidally averaged value and its deviation,

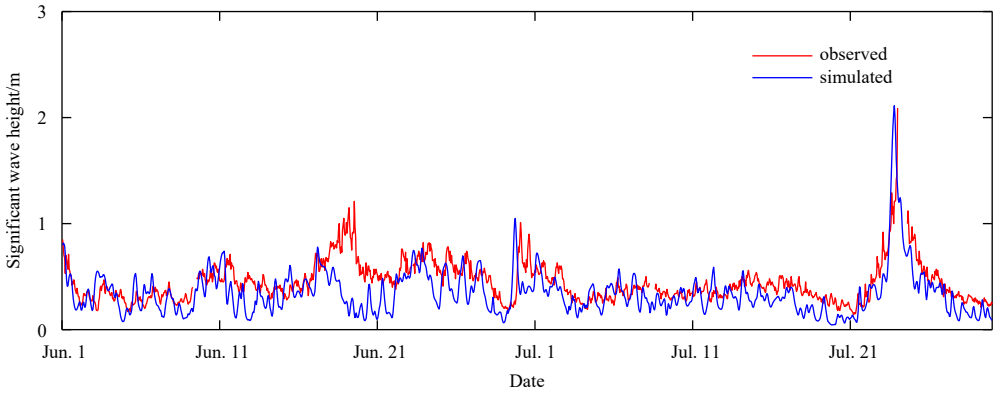

Fig. 3. Observed and simulated significant wave heights at Sta. W. The red and blue lines represent the observed and simulated results, respectively.

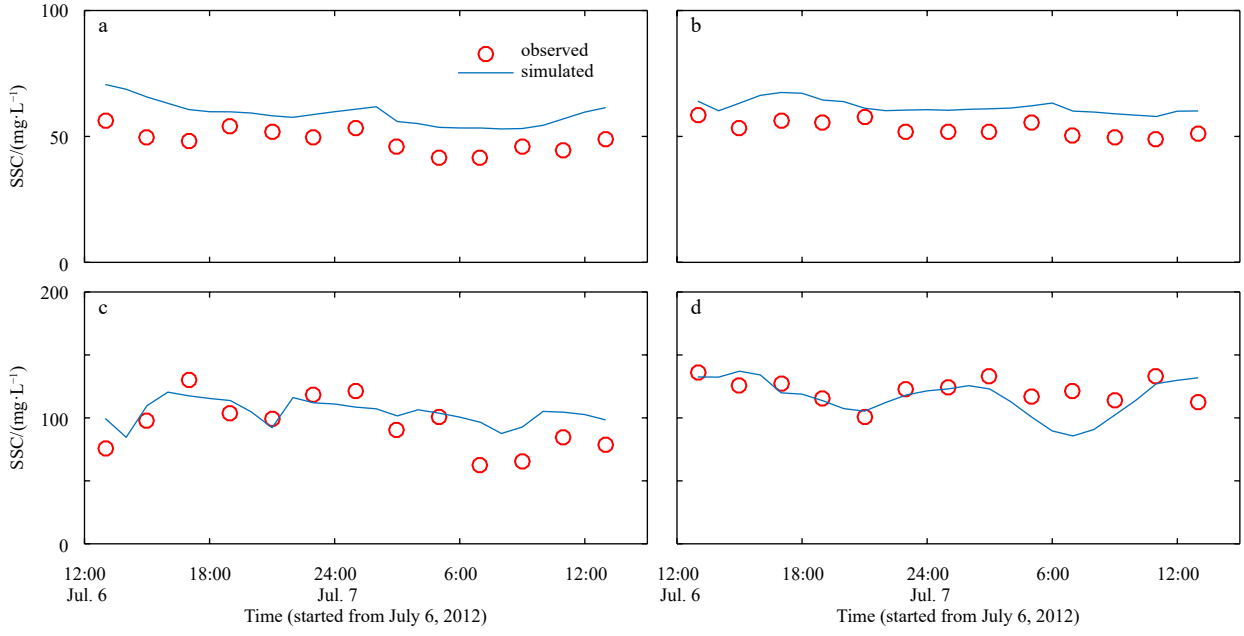

Fig. 4. Observed and simulated SSC at Sta. V1 surface (a) and bottom (b) and at Sta. V2 surface (c) and bottom (d). The red hollow circles and the blue lines represent the observed and simulated results, respectively.

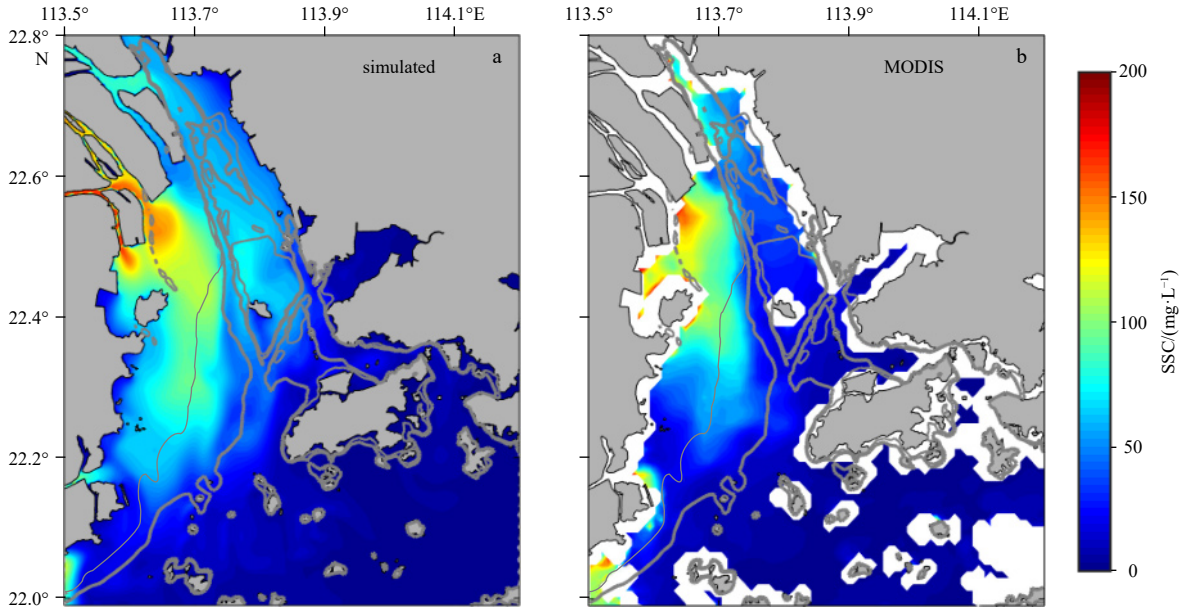

Fig. 5. Surface SSC distributions obtained from the model results (a) and moderate resolution imaging spectroradiometer (MODIS) data (b) on June 28, 2012. Thin/thick gray lines denote 6 m/8 m isobaths.

Table 4. Skill scores by comparison of modeled results with observations

Station	Parameter	SK
V1	SSC (surface and bottom)	0.56
V2	SSC (surface and bottom)	0.77
W	significant wave height	0.82

$$\begin{cases} \overline{u} = \overline{u}_0 + \overline{u}_t \\ \overline{c} = \overline{c}_0 + \overline{c}_t \\ \overline{u}_0 = \dfrac{1}{T}\displaystyle\int_0^T \overline{u}\cdot \mathrm{d}t \\ \overline{c}_0 = \dfrac{1}{T}\displaystyle\int_0^T \overline{c}\cdot \mathrm{d}t \end{cases}, \tag{3}$$

where T is the tidal period and $\overline{u}_0$ and $\overline{c}_0$ are the mean values of the vertically averaged velocity and sediment concentration over the tidal cycle, respectively. $\overline{u}_t$ and $\overline{c}_t$ are the corresponding deviations of vertically averaged values from the means.

The instantaneous sediment transport flux through a unit width of a section can be written as

$$F = \int_0^h u\cdot c\cdot \mathrm{d}z = \int_0^1 h\cdot u\cdot c\cdot \mathrm{d}\sigma, \tag{4}$$

where σ=z/h and σ is the relative depth from the seabed (σ=0) to the water surface (σ=1). The net sediment flux over a tidal cycle can be derived as

$$\begin{aligned} \langle F\rangle = \frac{1}{T}\int_0^T\int_0^1 (h_0+h_t)(\overline{u}_0+\overline{u}_t+u_v)(\overline{c}_0+\overline{c}_t+c_v)\,\mathrm{d}\sigma\mathrm{d}t = \\ h_0\overline{u}_0\overline{c}_0 + \overline{c}_0\langle h_t\overline{u}_t\rangle + \overline{u}_0\langle h_t\overline{c}_t\rangle + h_0\langle\overline{u}_t\overline{c}_t\rangle + \langle h_t\overline{u}_t\overline{c}_t\rangle + \\ h_0\langle\overline{u_vc_v}\rangle + \langle h_t\overline{u_vc_v}\rangle = T_1+T_2+T_3+T_4+T_5+T_6+T_7, \end{aligned} \tag{5}$$

where the brackets < > indicate tidally averaged values of vertical integrated variables, over bars denote the vertical averaged values, $h = h_0 + h_t$, h_0 and h_t are tidally averaged water depth and its deviation, respectively. T_1 and T_2 are the fluxes due to non-tidal drift (Eulerian velocity) and Stokes drift, respectively. T_3, T_4, and T_5 are the tidal pumping terms that are produced by tidal phase differences (Dyer, 1974). T_6 represents the gravitational circulation term, arising from the correlation between the bottom landward mean flow with high SSC and the surface seaward mean flow with lower SSC. T_7 arises from the changing forms of the vertical profiles of velocity and concentration within tidal period, and its magnitude is generally small. In this study, T_1, T_2, T_3+T_4+T_5, and T_6 are named Eularian, Stokes, tidal pumping, and vertical shear transport, respectively.

3 Results

3.1 *Effects of shoreline and bathymetry changes on SSC and sediment transport*

Figure 6 shows the distributions of tidally and vertically averaged bottom stress in spring tide in the 1971, transition, and 2012 cases, and Fig. 7 shows the distributions of vertically averaged SSC and depth-integrated sediment transport rate (STR) during this period. In the 1971 case, generally speaking, the current-induced bottom stress is similar to the wave-induced bottom stress. Near the outlets, due to the strong current, the current-induced bottom stress is greater than 1 Pa and greater than the wave-induced bottom stress. It is also significantly greater than the wave-induced bottom stress in the EC, WC, and MS, however, it is less than the wave-induced bottom stress in the WS downstream and MS (Figs 6d and g).

Compared with the 1971 case in spring tide, the current-induced bottom stress near the outlets increases in the transition case whose shoreline is changed, which is due to the increase in residual current owing to the narrow outlets (Figs 6d, e, 7a and b). Meanwhile, it decreases in the WS downstream and the MS, whilst the wave-induced bottom stress changes little, except that it decreases in the MS (Figs 6g and h). In general, except near the outlets, the wave-current combined bottom stress decreases in the WS, MS, ES, and EC of the ZRE (Figs 6a and b). In the WS, the area of SSC greater than 100 mg/L decreases by approximately

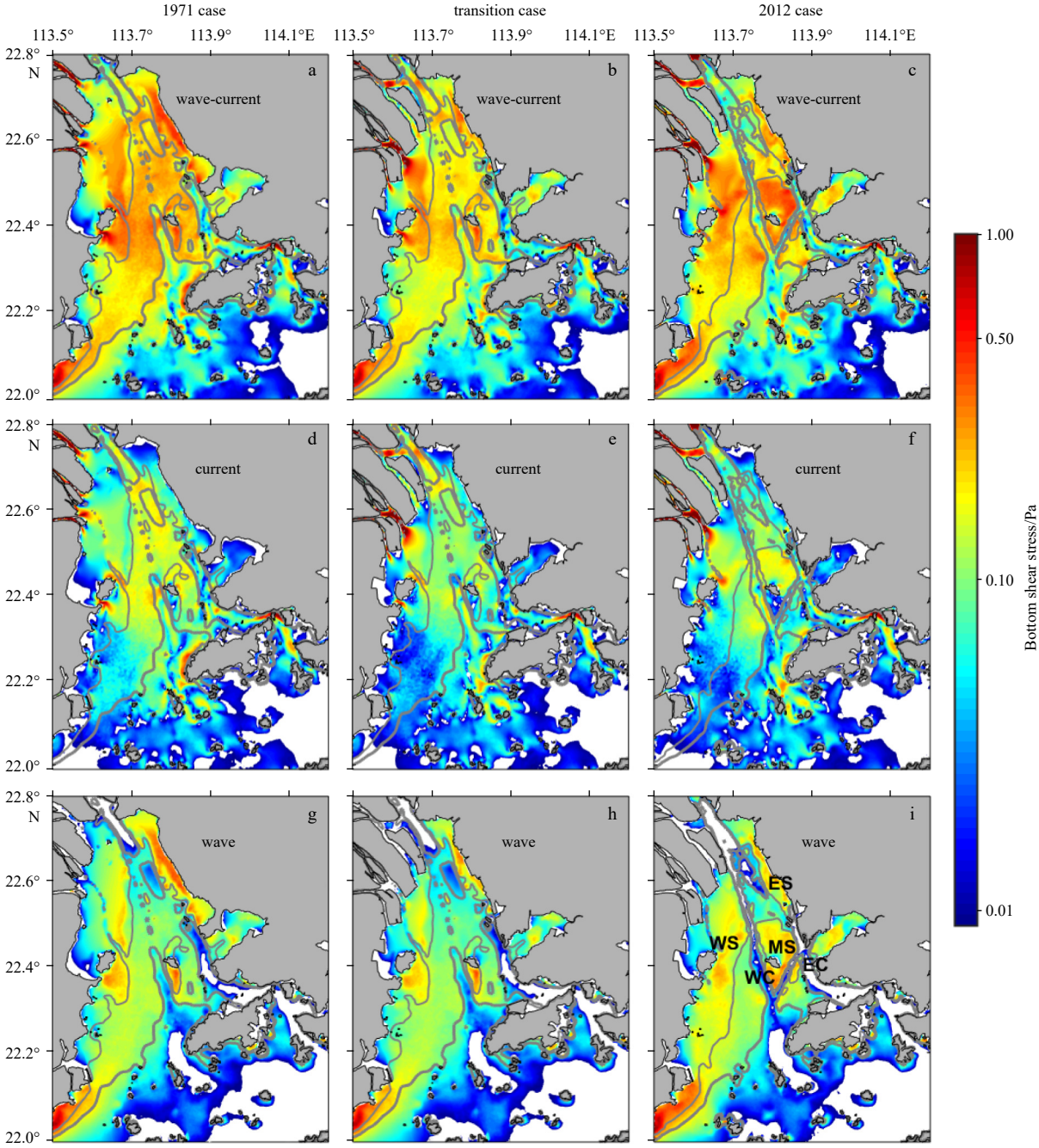

Fig. 6. Tidal averaged bottom shear stress in spring tide. a–c. Wave-current combined, d–f. current-induced, and g–i. wave-induced. Note that the bottom shear stress is on a log scale. The white areas correspond to bottom stress below 0.01 Pa. Thin/thick gray lines indicate 6 m/8 m isobaths. The 1971, transition and 2012 cases are indicated in the left, middle and right panels, respectively.

55.5 km^2, accounting for 17.8%, and moves eastward and southward 1–6 km (Figs 7a, b, and d). However, the SSC increases by 5–30 mg/L from downstream to upstream, and the seaward sediment transport is enhanced, owing to the closer sediment source to the offshore and the stronger residual current at the HEM and HQL outlets (Figs 7f, g, and i). The reclamation of LXI transports more sediment from the JM outlet eastward, which increases SSC and sediment transport on its east side and ES but decreases the SSC and sediment transport on its west and south sides. The SSC in the MS and EC changes little, whilst the seaward sediment transport in the EC decreases (Figs 7a, b, d, g, h, and i).

Compared with the transition case in spring tide, in the 2012 case whose bathymetry is changed, the current-induced bottom stress changes little (Figs 6e and f). However, the wave-induced bottom stress decreases greatly in the WC and EC due to channel deepening but increases in the WS and MS caused by silitation, resulting in an enhancement of wave-current bottom stress in the WS and MS. Therefore, the SSC in the WS further increases by 5–10 mg/L, and the area of SSC greater than 100 mg/L increases by 11.4% and expands eastward and southward (Figs 7b and c). The seaward sediment transport is notably strengthened by 19.86% in the WC and its west slope (Figs 7g, h and j). The SSC decreases in the MS (Fig. 7e), indicating that the deepening of WC restrains eastward sediment transport from lateral outlets

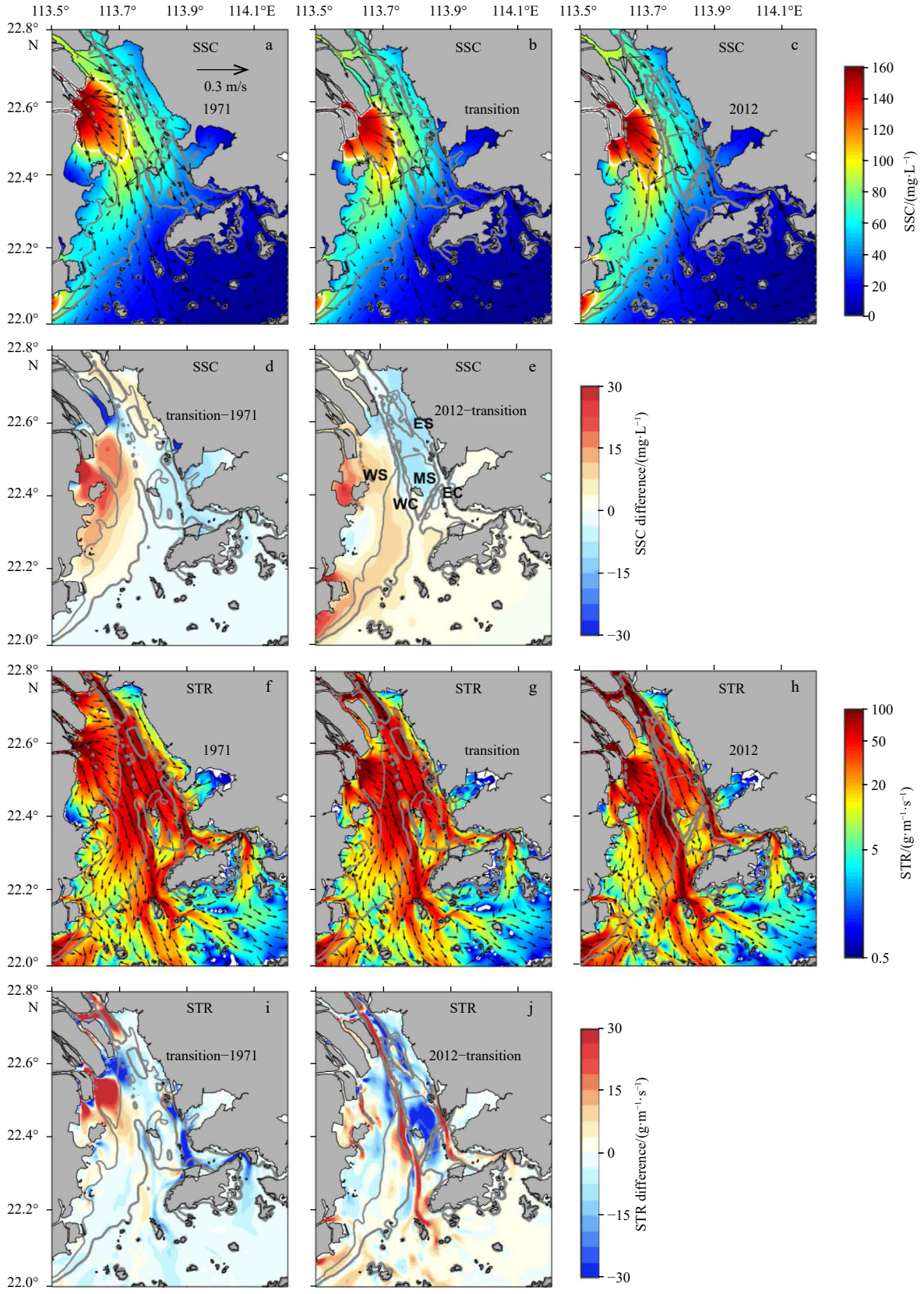

Fig. 7. Distributions of tidally and vertically averaged SSC (contour) and residual current (arrow), and tidally averaged and depth-integrated bottom shear stress in spring tide: a and f. 1971 case, b and g. transition case, c and h. 2012 case, d and i. the difference calculated by the transition case–1971 case, and e and j. the difference calculated by 2012 case–transition case. The arrows in f–h indicate the direction of bottom shear stress, and white areas indicate STR below 0.5 g/(m·s). Thin/thick gray lines denote 6 m/8 m isobaths.

(HEM and HQL), which is similar to that in Zhang et al. (2019). The SSC in EC is nearly unchanged, but the STR increases by ~20 g/(m·s), which is caused by the increase in water depth. Downstream of the ZRE, the SSC increases by 5–10 mg/L, and the seaward sediment transport increases, indicating that the change in bathymetry is conducive to seaward sediment transport.

In neap tide, the distributions of bottom stress, SSC, and STR of the three scenarios (1971, transition, and 2012 cases) are shown in Figs 8 and 9. In the 1971 case, the current-induced bottom stress is significantly weaker than that in spring tide (Figs 6a and 8a), and it is about 0.2 Pa near outlets and in the WC and EC. In contrast, the wave-induced bottom stress is larger in shallow areas, such as WS, MS, and ES (Figs 8a, d and g). The SSC is visibly smaller than that in spring tide, the area of SSC greater than 100 mg/L decreases to 86.5 km^2 (Table 5), and the STR also decreases. The residual current changes to landward in the WC and EC, leading to a landward sediment transport there (Figs 9a and f).

Compared with the 1971 case in neap tide, the current-induced bottom stress near the outlets increases in the transition case whose shoreline is changed. The current-induced bottom stress is enhanced in the WS upstream and east of LXI. The wave-induced bottom stress is reduced in the WS upstream, MS, and ES. Overall, the wave-current combined bottom stress is weakened in the WS upstream (Figs 8a and b). The area of SSC greater than 100 mg/L decreases by 11% (Table 5) and moves eastward and southward, which is similar to that in spring tide.

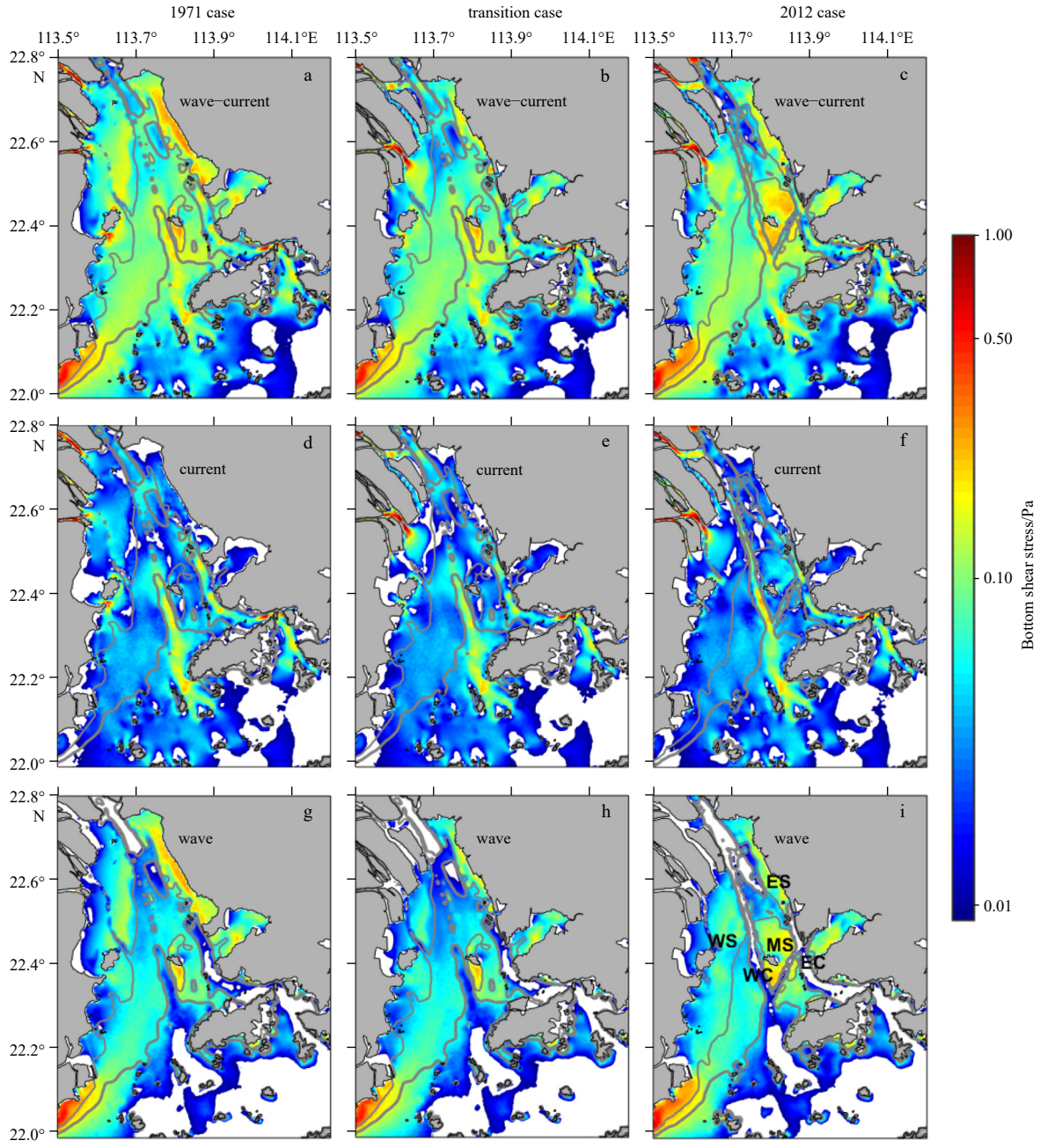

Fig. 8. Tidal averaged bottom shear stress in neap tide. a–c. Wave-current combined, d–f. current-induced, and g–i. wave-induced. Note that the bottom shear stress is on a log scale. The white areas correspond to bottom stress below 0.01 Pa. Thin/thick gray lines indicate 6 m/8 m isobaths. The 1971, transition and 2012 cases are indicated in the left, middle and right panels, respectively.

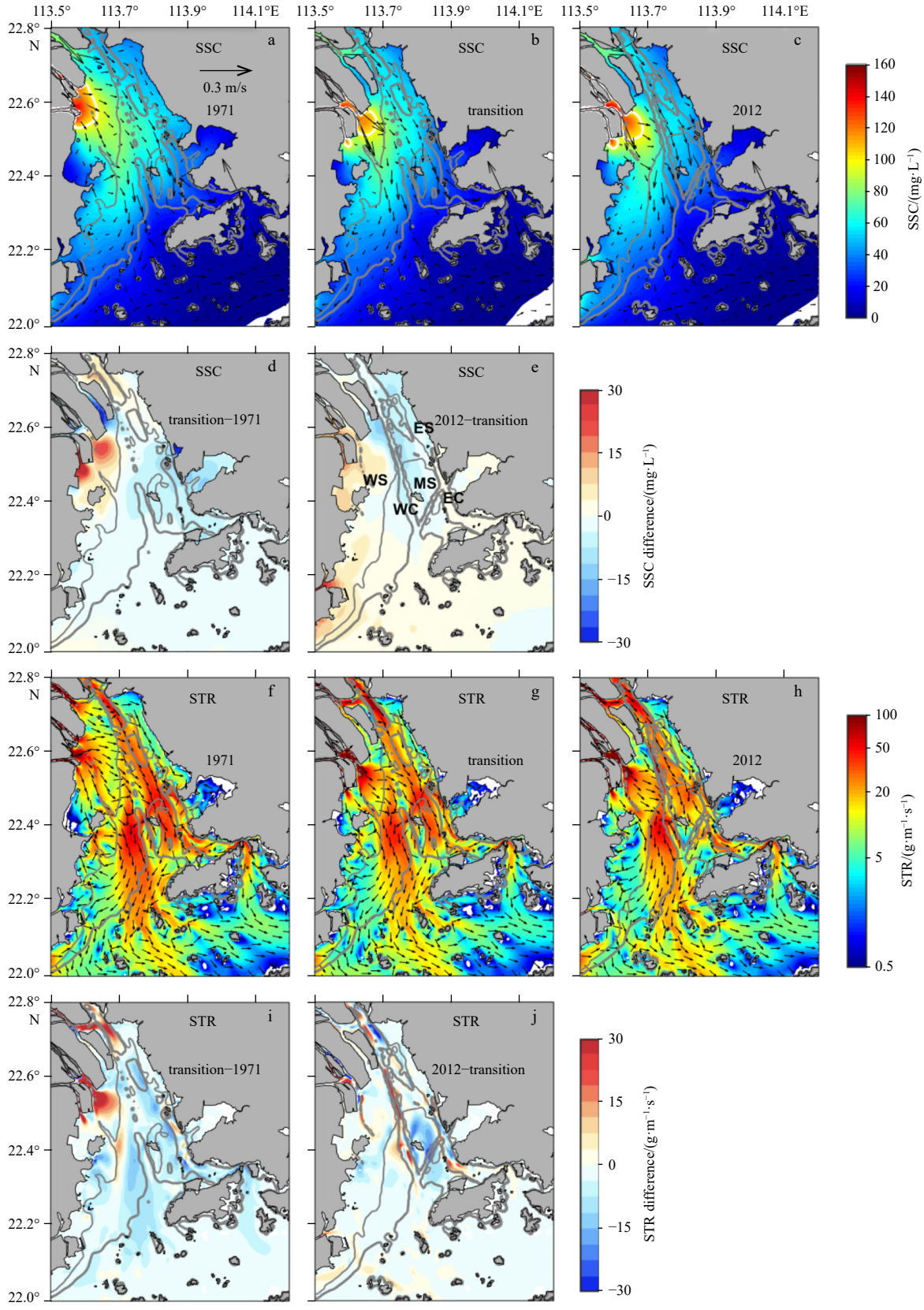

Fig. 9. Distributions of tidally and vertically averaged SSC (contour) and residual current (arrow), and tidally averaged and depth-integrated STR in neap tide: a and f. 1971 case, b and g. transition case, c and h. 2012 case, d and i. the difference calculated by the transition case–1971 case, and e and j. the difference calculated by 2012 case–transition case. The arrows in f–h indicate the direction of STR, and white areas indicate STR below 0.5 g/(m·s). Thin/thick gray lines denote 6 m/8 m isobaths.

Table 5. Areas with depth-averaged SSC greater than 100 mg/L in spring and neap tides in the three scenarios

Period	Model scenarios	Area/km^2
Spring	1971 case	314.4
	transition case	255.9
	2012 case	284.3
Neap	1971 case	81.5
	transition case	77.0
	2012 case	88.3

Note: The spring and neap tide periods are denoted by dark and light gray shadows in Fig. 2c, respectively.

The SSC in the WS upstream increases by 5–20 mg/L, and the seaward sediment transport is strengthened. The SSC increases on the east side of LXI but decreases on the south side.

Compared with the transition case in neap tide, in the 2012 case that bathymetry is changed, the current-induced bottom stress changes little, except that it increases in the WC (Figs 8e and f). The wave-induced bottom stress is weakened in the WC and EC, whilst it is enhanced in the WS and MS (Figs 8b–d, f, h and i). In the WS, the area of SSC greater than 100 mg/L increases by 6.8% and moves eastward and southward. Upstream of the ZRE except in the WS, the SSC is reduced by 5–10 mg/L. However, downstream of the ZRE, the SSC is enhanced. In the WC, the landward sediment transport is strengthened due to the landward residual current.

In general, the change in shoreline increases the current-induced bottom stress near the outlets and makes the sediment source closer to the offshore. The SSC in the WS and east side of LXI increases, and the seaward sediment transport is enhanced. The change in bathymetry increases the wave-induced bottom stress of the WS, MS, and ES, increasing the SSC in the WS. However, the SSC in the MS and ES is reduced because the sediment from the HEM and HQL outlets cannot cross the WC, and the reason will be analyzed in Section 4.2. Downstream of the ZRE, the SSC increases, and the seaward sediment transport also increases.

3.2 *Variations in SSC and sediment transport in deep channels*

To explore the impact of shoreline and bathymetry changes on suspended sediment transport in deep channels, we select longitudinal Section A (shown in Fig. 1e) in the WC for analysis. Figure 10 shows the along-channel distributions of tidally averaged SSC, salinity, longitudinal residual current, and bottom stress in spring tide in the three scenarios. The x-axis represents the distance from the southern end of Section A. In the 1971 case, the maximum SSC is about 96 mg/L, and the ETM is located at approximately x=60 km near the saltwater wedge (Fig. 10a), which is consistent with previous conclusions (Wai et al., 2004). There is a vertical circulation in a surface seaward and bottom landward pattern (Fig. 10d). The main component of the bottom stress is the current-induced bottom stress, whilst the wave-induced bottom stress reaches 0.2 Pa only at the shallow area upstream (Fig. 10g). When the riverine sediments input from outlets are transported to the deep channel, they are resuspended by wave-current combined bottom stress and then transported to the saltwater wedge by vertical circulation, as suggested by Liu et al. (2018).

Compared with the 1971 case in spring tide, the SSC changes little in the transition case whose shoreline is changed, but the ETM moves southward about 6 km (Figs 10a and b). The bottom isohaline extends landward 2–5 km, while the surface isohaline changes little so that the isohaline is more horizontal and the baroclinic gradient is enhanced, slightly increasing the vertical circulation (Figs 10a, b, d and e). The wave-induced bottom stress changes little, while the current-induced bottom stress upstream decreases by about 0.2 Pa. Therefore, the reduction in current-induced bottom stress and the strengthening of vertical circulation cancel each other out, resulting in a small change in the SSC.

Compared with the transition case in spring tide, in the 2012

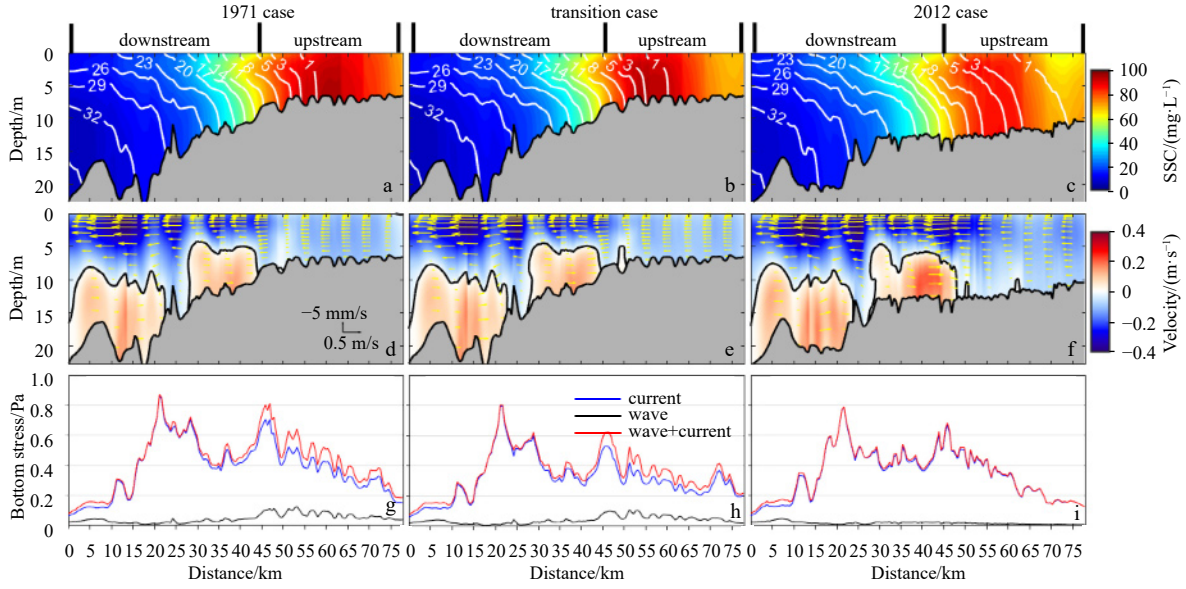

Fig. 10. Along-channel distributions of tidally averaged SSC (contours) and salinity (white lines) (a, b, c), along-channel residual current (contours and arrows) (d, e, f), and bed shear (g, h, i) at Section A (shown in Fig. 1e) in spring tide. The positive value for the along-channel residual current is landward, and the zero along-channel residual current is marked by a black solid line. The current-induced, wave-induced and wave-current combined bottom shear stresses are denoted by blue, dark, and red lines, respectively. The 1971, transition and 2012 cases are indicated in the left, middle and right panels, respectively.

case whose bathymetry is changed, the location of the ETM is unchanged, but the maximum SSC decreases from 96.13 mg/L to 86.07 mg/L (Figs 10b and c). The bottom isohaline intrudes landward about 3 km, and the salinity difference between the surface and bottom layers increases, leading to a larger baroclinic pressure gradient and vertical circulation (Figs 10e and f). Moreover, the current-induced bottom stress is also weakened (Figs 10h and i). However, these changes do not increase the SSC. Thus, the decrease in SSC is caused by a smaller wave-induced bottom stress.

In neap tide, in the 1971 case, the location of the ETM is close to that in spring tide, and the maximum SSC is 80.34 mg/L. The salinity difference between the surface and bottom layers increases compared with the spring tide. Thus, the baroclinic pressure gradient increases, and the vertical circulation is streng thened (Figs 10a, d, 11a and d).

Compared with the 1971 case in neap tide, in the transition case whose shoreline is changed, the position of the ETM and the maximum SSC changes little, but the area of SSC greater than 60 mg/L is reduced. The bottom isohaline intrudes landward about 2 km, and the surface isohaline extends seaward 2–5 km and consequently increases the vertical circulation, which is similar to that in spring tide (Figs 11a, b, d and e). The wave-induced bottom stress changes little, but the current-induced bottom stress decreases by about 0.2 Pa (Figs 11g and h). Therefore, the decrease in SSC is caused by the reduction in current-induced bottom stress in neap tide.

Compared with the transition case in spring tide, in the 2012 case with bathymetry change, the location of the ETM moves north ward ~5 km, the SSC is reduced, and its peak value is 75.28 mg/L (Figs 11b and c). The bottom isohaline intrudes landward notably, and the vertical circulation is strengthened significantly (Figs 11e and f). The current-induced bottom stress is enhanced, but the wave-induced bottom stress weakens. Thus, the reduction in SSC is attributed to the smaller wave-induced bottom stress.

Generally, at Section A in the WC, the change in shoreline makes the SSC change slightly in spring tide since the enhancement of vertical circulation is offset by the reduction in current-induced bottom stress. However, the effect of reduction on current-induced bottom stress is stronger in neap tide, resulting in a smaller area of SSC greater than 60 mg/L. The change in bathymetry decreases the SSC whether in spring tide or neap tide, both due to the reduction in wave-induced bottom stress.

3.3 *Cross-channel variations in SSC and sediment transport*

To explore the impact of shoreline and bathymetry changes on lateral sediment transport, we select cross-channel Section B (shown in Fig. 1e) for analysis. The cross-channel distributions of tidally averaged SSC, salinity, cross-channel residual current, and bottom stress in spring are shown in Fig. 12. The 0 km on the *x*-axis is from the west. In the 1971 case, the maximum SSC is 108.75 mg/L in the WS near *x*=11 km (Fig. 12a). The cross-channel current is eastward in the surface layer and irregular in the bottom layer (Fig. 12d). The wave-induced bottom stress is less than the current-induced bottom stress (Fig. 12g).

Compared with the 1971 case in spring tide, in the transition case whose shoreline is changed, the SSC increases with the peak value increasing by 16.3% to 126.51 mg/L, but the location of the maximum SSC is unchanged. The current-induced bottom stress is reduced in the WS, and the maximum value decreases from 0.85 Pa to 0.56 Pa (Figs 12g and h), indicating that the increase in SSC is caused by the seaward extension of the sediment source and the stronger residual current at the HEM and HQL outlets. For the same reason, the SSC in the WC (near *x*=55 km at Section A) and MS increases, which is consistent with the southward movement of the ETM in the WC.

Compared with the transition case in spring tide, in the 2012

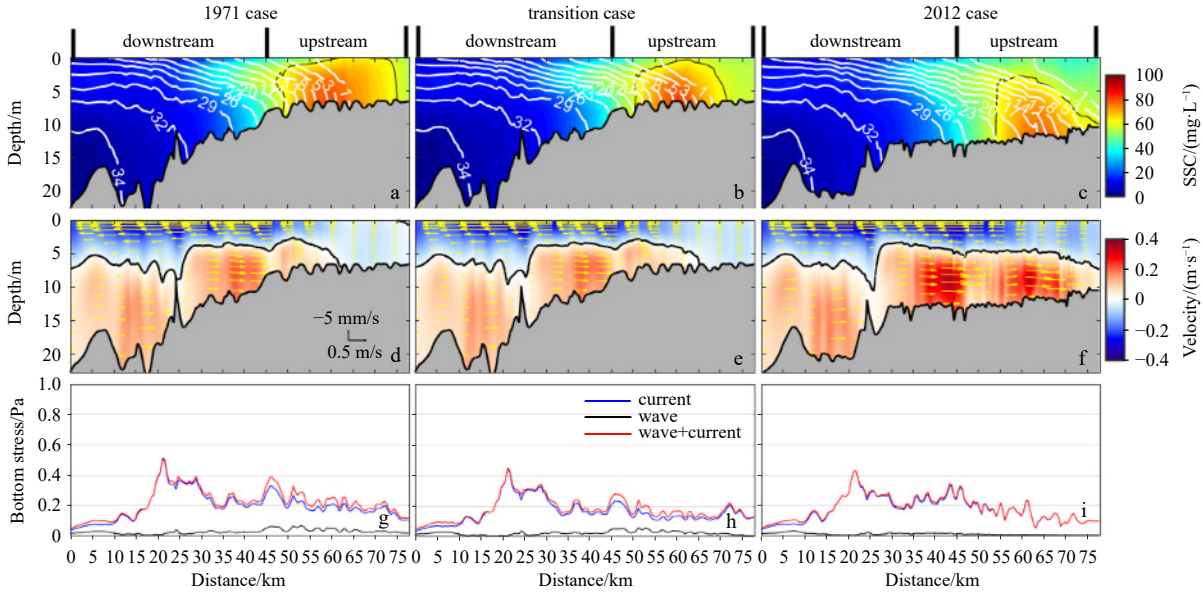

Fig. 11. Along-channel distributions of tidally averaged SSC (contours) and salinity (white lines) (a, b, c), along-channel residual current (contours and arrows) (d, e, f), and bed shear (g, h, i) at Section A (shown in Fig. 1e) in neap tide. The positive value for the along-channel residual current is landward, and the zero along-channel residual current is marked by a black solid line. The current-induced, wave-induced and wave-current combined bottom shear stresses are denoted by blue, dark, and red lines, respectively. The SSC of 60 mg/L is marked by a black solid line in a, b and c. The 1971, transition and 2012 cases are indicated in the left, middle and right panels, respectively.

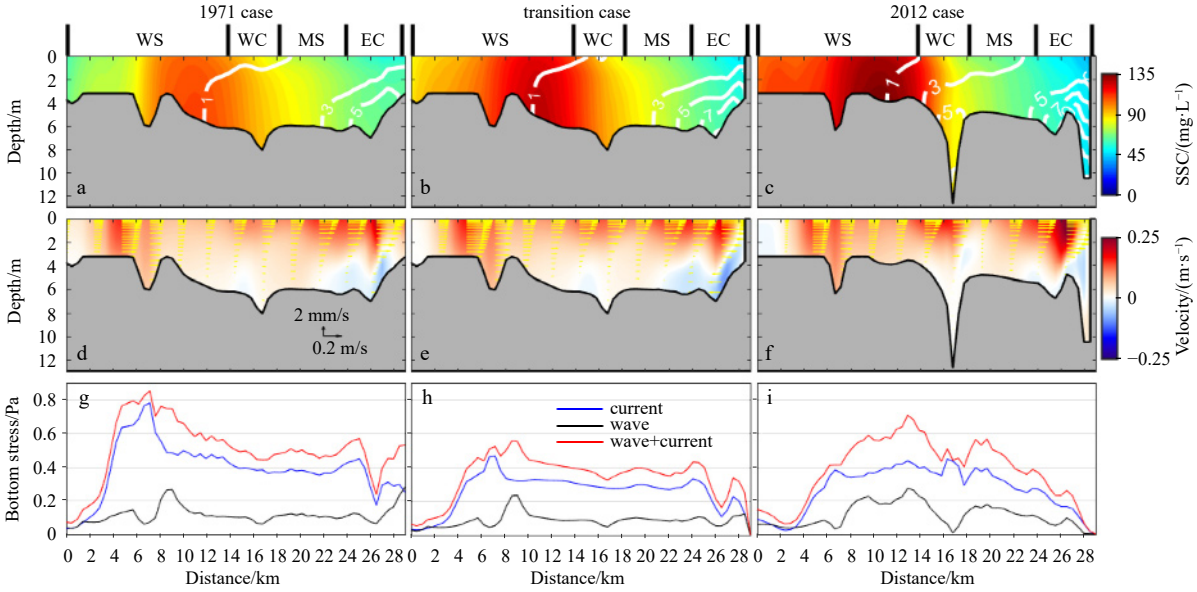

Fig. 12. Cross-channel distributions of tidally averaged SSC (contours) and salinity (white lines) (a, b, c), cross-channel residual current (contours and arrows) (d, e, f), and bottom stress (g, h, i) at Section B (shown in Fig. 1e) in spring tide. In a–c, the isohalines are plotted every 2 psu. The positive value for the cross-channel residual current is eastward. The current-induced, wave-induced and wave-current combined bottom stresses are denoted by blue, dark, and red lines, respectively. The 0 km on the *x*-axis is from the west, and the vantage point is looking in the estuary. The 1971, transition, and 2012 cases are indicated in the left, middle and right panels, respectively.

case whose bathymetry is changed, although the position of the maximum SSC in the WS remains unchanged, the peak value increases by 6.2% to 134.39 mg/L (Figs 12b and c), which is caused by the enhancement of wave-induced bottom stress (Figs 12h and i). In the WC, the SSC is reduced owing to the smaller wave-induced bottom stress, as analyzed above. The deepening of the WC restrains eastward sediment transport, leading to a reduction in SSC in the MS and EC. In neap tide, the situation at Section B is similar to that in spring tide (figure omitted), but the SSC and bottom stress are reduced.

Overall, the change in shoreline increases the SSC at lateral Section B, caused by the closer sediment source to the offshore and the stronger residual current at the HEM and HQL outlets. The change in bathymetry increases the SSC in the WS, caused by the increase in wave-induced bottom stress. However, it decreases the SSC in the WC, MS, and EC since the deepening of WC restrains eastward sediment transport, which will be analyzed in Section 4.2.

4 Discussion

4.1 *Decomposition of longitudinal suspended sediment flux*

The decomposition results of longitudinal suspended sediment flux, obtained by Eq. (5), along Section A are shown in Fig. 13. In the 1971 case in spring tide, the total sediment flux is seaward. The Eulerian transport T_1 is dominant, and its maximum value is at x=61 km near the ETM, reaching –94 g/s. The Stokes transport T_2 is landward with a maximum value of 14 g/s. The tidal pumping transport including T_3+T_4+T_5 is landward upstream, with a maximum of 12 g/s. The vertical shear transport T_6 is seaward downstream and close to 0 upstream (Fig. 13d). Therefore, the formation of ETM in the WC is mainly caused by Eulerian transport T_1 and tidal pumping transport including T_3+T_4+T_5.

Compared with the 1971 case in spring tide, the decomposition of suspended sediment flux is similar in the transition case whose shoreline is changed (Figs 13d and e). However, the maximum seaward Eulerian transport T_1 moves southward approximately 6 km (Figs 13d and e), which may explain why the ETM in the WC moves southward 6 km.

Compared with the transition case in spring tide, in the 2012 case whose bathymetry is changed, the seaward Eulerian transport T_1 in the upstream increases notably by 109.88%, and the landward Stokes transport T_2 and tidal pumping transport including T_3+T_4+T_5 are also strengthened there but much weaker than T_1. Therefore, the SSC in the ETM is reduced.

In neap tide of the 1971 case, the total suspended sediment flux is changed from seaward to landward at 35–43 km and 46–55 km, dominated by Eulerian transport T_1 (Figs 13d and g). The Stokes transport T_2 is similar to that in spring tide but weaker. The influence of tidal pumping transport including T_3+T_4+T_5 is also weaker. The vertical shear transport T_6 is similar to that in spring tide. Among all of the landward fluxes, Eulerian transport T_1 is the largest, and the other terms are smaller, indicating that the formation of ETM is mainly attributed to Eulerian transport.

Compared with the 1971 case in neap tide, the decomposition of suspended sediment flux in the transition case whose shoreline is changed is similar, which is dominated by Eulerian transport T_1 (Figs 13g and h).

Compared with the transition case in neap tide, in the 2012 case whose bathymetry is changed, the landward Eulerian transport T_1 upstream increases to 102 g/s, the Stokes transport T_2 changes little, the tidal pumping transport including T_3+T_4+T_5 increases slightly upstream, and the vertical shear transport T_6 increases significantly due to the strengthened vertical circulation (Figs 13h and i). Thus, the ETM moves upstream, and the formation of the ETM is mainly attributed to Eulerian transport T_1 and vertical shear transport T_6.

Generally, in the 1971 case in spring tide, the mechanism of

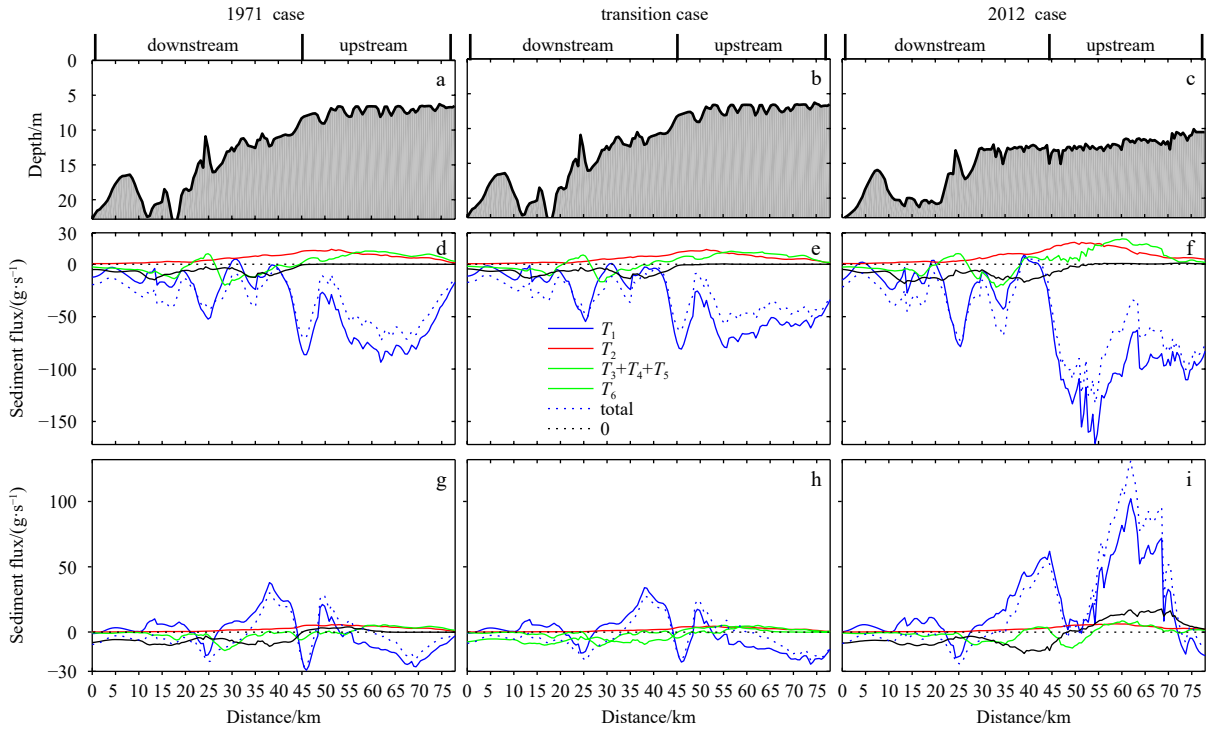

Fig. 13. Along-channel bottom bathymetries (a, b, c) and along-channel distributions of tidally averaged sediment fluxes in spring tide (d, e, f) and neap tide (g, h, i) at Section A (shown in Fig. 1e). T_1, T_2, T_3+T_4+T_5, and T_6 represent Eulerian transport, Stokes transport, tidal pumping transport, and vertical shear transport, respectively.

ETM formation in the WC is due to the Stokes transport T_2 and tidal pumping transport including T_3+T_4+T_5. The change in shoreline makes the maximum value of seaward Eularian transport T_1 at 60 km move southward by about 5 km, so does the ETM move southward by 5 km. The change in bathymetry significantly increases the seaward Eularian transport T_1 upstream by 109.88%, causing less SSC in the WC. In the 1971 case in neap tide, the formation of ETM is primarily due to Eularian transport. The change in shoreline does not change the sediment decomposition fluxes. However, the change in bathymetry notably increases the upstream Eulerian transport T_1 to 102 g/s and significantly strengthens the vertical shear transport T_6, so the ETM moves northward.

4.2 *Decomposition of lateral suspended sediment flux*

The decomposition results of lateral suspended sediment flux, obtained by Eq. (5), along Section B are shown in Fig. 14. In spring tide, in the 1971 case, the lateral suspended sediment flux is mainly controlled by the eastward Eularian transport T_1, whilst the other terms contributes little. The peak value of T_1 is ~50 g/s near x=7 km (Fig. 14d).

Compared with the 1971 case in spring tide, the decomposition of suspended sediment flux in the transition case whose shoreline is changed is similar, but with a larger Eularian transport T_1 in the WS and WC at 2–18 km (Figs 14d and e), increasing the eastward sediment transport. Thus, the SSC is strengthened there, as well as in the MS.

Compared with the transition case in spring tide, in the 2012 case, the Eularian transport T_1 increases in the WS and WC at 6–16 km, which increases the total sediment flux and SSC here (Figs 14e and f). However, on the east side of the WC at 16 km, the Eularian transport T_1 decreases significantly and the total flux decreases, so there is less sediment transport eastward. That is, the deepening of WC restrains eastward sediment transport by reducing eastward Eulerian transport, resulting in a smaller SSC in the MS. The results in neap tide are similar to those in spring tide but weaker, and the change in bathymetry makes the sediment transport westward in the WC (Figs 14g, h and i).

Overall, the change in shoreline increases the Eulerian transport in the WS and WC, and then the total eastward transport is enhanced, increasing the SSC there. The change in bathymetry restrains eastward sediment transport by reducing eastward Eulerian transport T_1.

4.3 *Wave effects on SSC and sediment transport in the wet season*

To explore the impact of waves on SSC in the wet season, we select calm and wavy periods for analysis. The periods are denoted by blue and red shadows in Figs 2e and f, both of which are 25 hours. In spring tide, the tidally averaged significant wave heights during calm and wavy periods are 0.24 m and 0.65 m, respectively (Table 6). Figure 15 shows the tidally averaged bottom stresses during calm and wavy periods in spring tide. The wave-induced bottom stress is strong in shallow areas such as WS, MS, and MS but weak in deep areas, especially it is close to zero in the WC and EC. During the calm period, the wave-induced bottom stress is relatively small and lower than 0.10 Pa upstream, and it is generally less than the current-induced bottom stress (Figs 15b and c). During the wavy period, the current-induced bottom stress is close to that during the calm period, most of which are less than 0.20 Pa (Figs 15b and e). However, the wave-induced bottom stress increases significantly and is stronger than the current-induced bottom stress, and its value is greater than 1 Pa in WS, MS, and ES.

Figure 16 shows the distributions of tidally and vertically averaged SSC and the tidally averaged but depth-integrated STR. Compared with that in the calm period, the SSC is larger in the

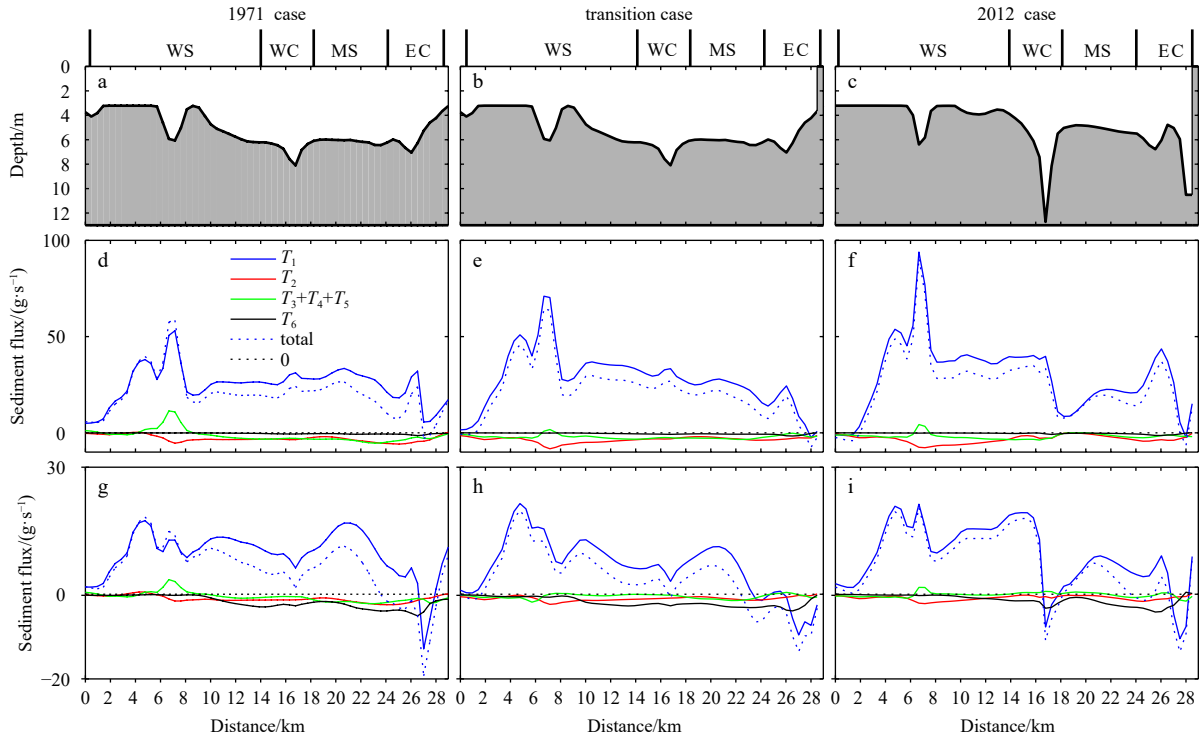

Fig. 14. Cross-channel bottom bathymetries (a, b, c) and cross-channel distributions of tidally averaged sediment fluxes in spring tide (d, e, f) and neap tide (g, h, i) at Section B (shown in Fig. 1e). T_1, T_2, T_3+T_4+T_5, and T_6 represent Eulerian transport, Stokes transport, tidal pumping transport, and vertical shear transport, respectively.

Table 6. Significant wave height and areas with depth-averaged SSC greater than 100 mg/L during calm and wavy periods in the 2012 case

Period	Wave condition	Significant wave height/m	Area/km^2
Spring	calm period	0.24	363.3
	wavy period	0.65	128.2
Neap	calm period	0.20	117.8
	wavy period	0.58	38.7

Note: The calm and wavy periods are presented by blue and red shadows in Figs 2e and f, respectively. The spring and neap tide periods are denoted by dark and light gray shadows in Fig. 2c, respectively.

wavy period. The area with SSC greater than 100 mg/L increases from 128.2 km^2 by 183.4% to 363.3 km^2 (Table 6), and the SSC in MS increases ~20 mg/L. During these two periods, the riverine runoff is close, at ~30 000 m^3/s (Fig. 2b). The wind forcing is also similar, with a southwest wind of 5–6 m/s (Fig. 2a). Moreover, the residual current is similar, which is larger near the entrance, reaching 0.3 m/s (Figs 16a and c). The runoff, wind forcing, and current-induced bottom stress are close, whilst the SSC increases during the wavy period, indicating that this is due to the increase in wave-induced bottom stress, which enhances resuspension. The suspended sediment transports seaward, and the increase in wave-induced bottom stress increases seaward sediment transport (Figs 16b and d).

The situation in neap tide is similar to that in spring tide (figure omitted). However, due to the weakening of tidal currents in neap tide, the current-induced bottom stress is reduced, and tidal scouring weakens, resulting in a reduction in SSC. Compared with that in the calm period, the area of SSC greater than 100 mg/L in the wavy period increases by 79.1 km^2, accounting for 204.4% (Table 6).

In conclusion, in the wet season, under the action of waves in wavy period, the wave-induced bottom stress cannot be ignored. It increases the resuspension of suspended sediment, resulting in a larger SSC, and strengthens seaward sediment transport.

4.4 *Comparison to other studies related to suspended sediment transport*

Zhang et al. (2021a) only studied the wave effects on sediment transport in the dry winter season in the ZRE, and found that waves increased the bottom stress, particularly at the shoal, and consequently the resuspension and SSC in the dry winter season. However, in the wet summer season, few studies investigated the wave effects on sediment transport deeply, although Liu and Cai (2019) considered the coupled wave-current effects on sediment transport in the ZRE, they did not study the influence of waves. In this study, we explore the wave effects on sediment transport in the wet season, and find that waves increase the bottom stress in the WS, leading to more resuspension and SSC. Thus, the area of SSC greater than 100 mg/L increases by 183.4% from 128.2 km^2 to 363.3 km^2. Moreover, we further study the wave effects on sediment transport under the conditions of changed shoreline and bathymetry. Zhang et al. (2019) simulated the transport and fate of multi-sourced sediments in the wet season in the ZRE and illustrated that riverine sediments from the lateral outlets (HEM and HQL) were mostly distributed in the WS and were inhibited from entering the WC, but they did not explain the related dynamic mechanism. This agrees with our conclusion in the 2012 case, however, this phenomenon does not occur in the 1971 and transition cases. Why? It is noticed that in the 1971 and transition cases, the water depths are the same, whilst in the 2012 case, the water depth deepens in the WC. Therefore, it is suggested that the deepening of WC restrains the eastward sediment transport owing to weakened eastward Eu-

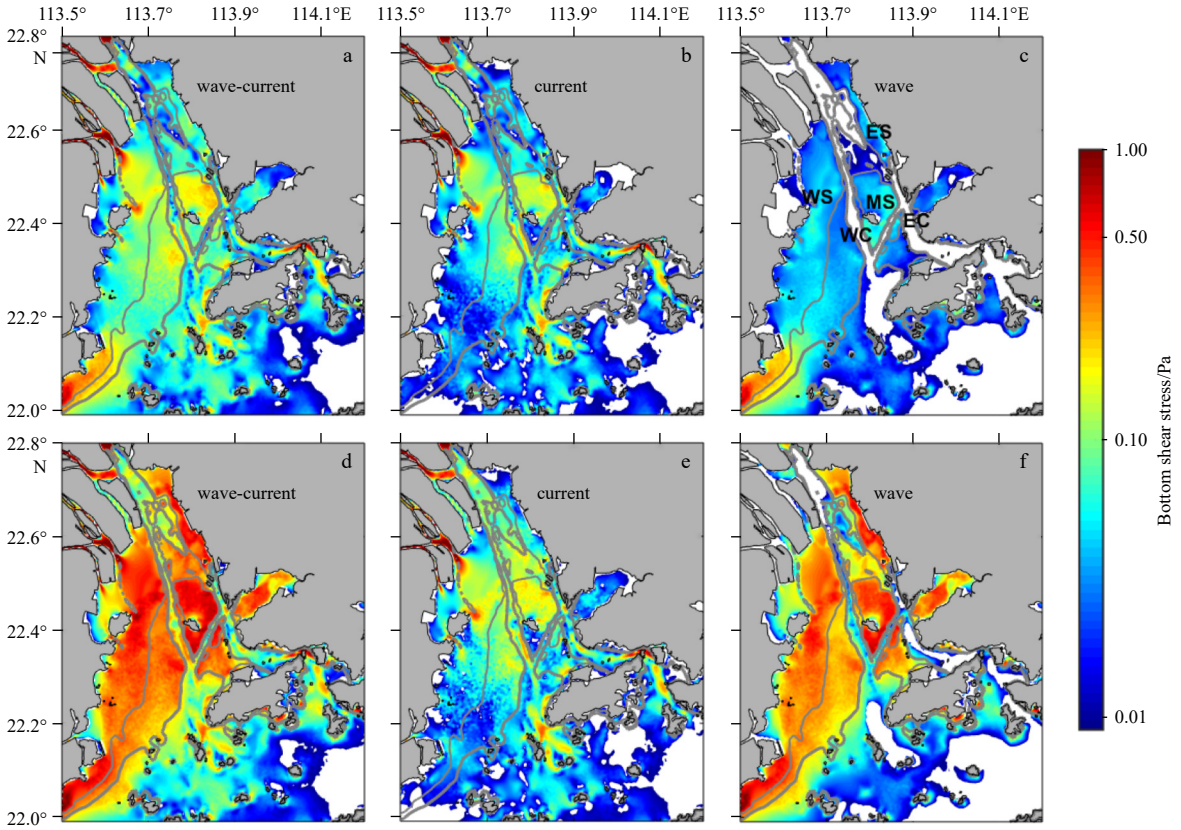

Fig. 15. Model results in spring tide in the 2012 case. Tidally averaged bottom stress during the calm period: a. wave-current combined, b. current-induced, c. wave-induced, and during the wavy period: d. wave-current combined, e. current-induced, f. wave-induced. The white areas correspond to bottom stress below 0.01 Pa. Thin/thick gray lines denote 6 m/8 m isobaths.

lerian transport on the east side of the WC.

There have been many previous studies on the influence of human interventions on suspended sediment distribution in the ZRE (Zhan et al., 2019; Wei et al., 2021). However, they did not separate the respective effects of the changes in shoreline and bathymetry. In this study, we consider the impact of the changes in shoreline and bathymetry separately, showing that they both reduce the range of the ETM in the WS but increase the SSC there in the condition that the changes in river runoff and riverine sediment load in the three scenarios are ignored, in fact, the runoff of the ZRE increases while the riverine sediment load decreases due to the sand excavation and dam construction (Dai et al., 2008; Tan et al., 2017). Therefore, this study is of important guiding significance for the impact of estuarine reconstruction (reclamation and dredging) on suspended sediment transport without considering the changes in incoming river discharge and riverine sediment.

It is interesting to compare our study with that in the Changjiang River Estuary. In the North Branch channel of Changjiang River Estuary, due to the drastic reduction in river width caused by land reclamation, the channel became increasingly flood-dominated from 1984 to 2011, increasing the landward sediment transport (Dai et al., 2016). However, in this study, the ZRE became increasingly ebb-dominated from 1978 to 2014 (Liu et al., 2020), and the reason for the increase of SSC in the WS is because the sediment source is closer to the offshore and the residual current is stronger at the HEM and HQL outlets.

5 Conclusions

To explore the response of suspended sediment transport to changes in shoreline and bathymetry in the wet season in the ZRE, a wave-current-sediment coupled numerical model is employed in this paper, and 3 scenarios (1971 case, transition case, and 2012 case) are run. The modeled results are well validated by observations. The main conclusions are as follows:

(1) During the wavy period in spring tide, the SSC is larger than that in the calm period. The area of SSC greater than 100 mg/L increases by 183.4% from 128.2 km^2 to 363.3 km^2. Meanwhile, the SSC in the MS increases by nearly 20 mg/L. The increase in SSC is due to the large wave-induced bottom stress, which suspends more sediment. The results in neap tide are similar.

(2) The change in shoreline in spring tide reduces the area of SSC greater than 100 mg/L by 17.8% (55.5 km^2) in the WS, which moves 1–6 km eastward and southward, but the SSC there increases by 5–30 mg/L from downstream to upstream, which is because the sediment source is closer to the offshore and the residual current is stronger at the HEM and HQL outlets. The strengthened eastward Eulerian transport in the WS and WC increases the SSC there. The reclamation of LXI increases the SSC on its east side and ES but decreases the SSC on its west and south sides. In addition, due to the southward movement of the maximum longitudinal Eulerian transport in the WC, the ETM located near the saltwater wedge moves southward about 6 km. In neap tide, the changes are similar but relatively weaker, and the decrease in the area of SSC greater than 60 mg/L in the WC is caused by the smaller current-induced bottom stress.

(3) The change in bathymetry in spring tide makes the SSC in the WS increase by 5–10 mg/L, the area of SSC greater than 100 mg/L expand eastward and southward and increase by 11.4% due to the increases in wave-induced bottom stress and east-

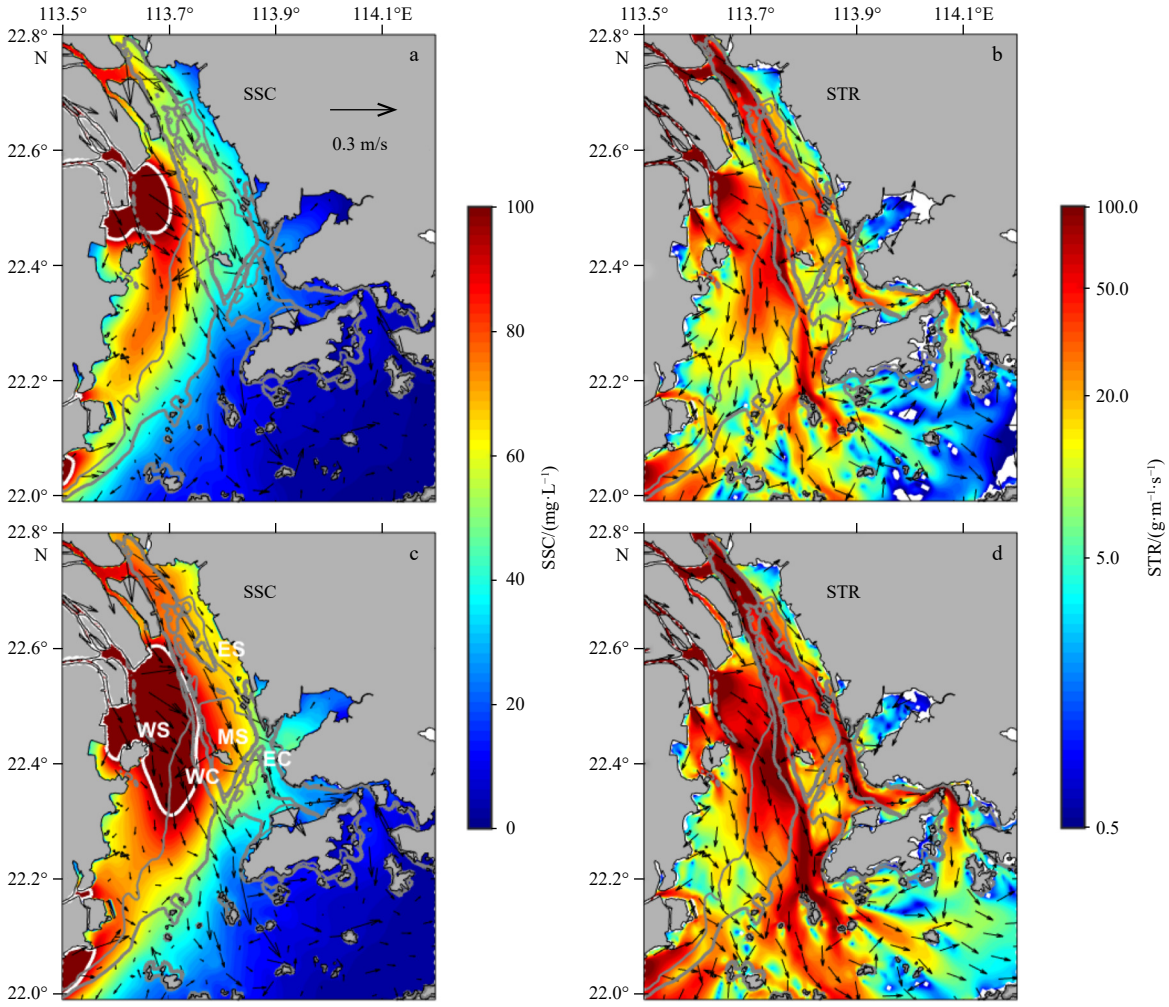

Fig. 16. Model results in spring tide in the 2012 case. Tidally and vertically averaged SSC (contour) and residual current (arrow) during the calm period (a) and wavy period (c). Tidally averaged and depth-integrated sediment transport rate (STR; unit: g/(m·s)) during the calm period (b) and wavy period (d). The arrow indicates the direction of the STR, and the white areas indicate an STR below 0.5 g/(m·s). Thin/thick gray lines denote 6 m/8 m isobaths.

ward Eulerian transport. The SSC is reduced in the MS owing to the weakened eastward Eulerian transport on the east side of the WC, that is, the deepening of WC inhibits eastward sediment transport. Moreover, the maximum SSC in the WC is reduced by 10.5%, caused by the smaller wave-induced bottom stress and a significant increase of 109.88% in southward Eulerian transport. The results in neap tide are similar to those in spring tide but with smaller changes. In the WC, the northward sediment transport is due to the northward Eulerian transport and vertical shear transport.

This study has implications in the sediment transport in the ZRE and other estuaries worldwide affected by human interventions, and it may help to expand the scientific cognition of the responses of marine water quality and deposition environment in the ZRE under the influence of human interventions such as reclamation and dredging, and provide some references for marine ecological environment security and coastal management in the ZRE.

Acknowledgements

The numerical simulation is supported by the High Performance Computing (HPC) Division and HPC managers of Wei Zhou and Dandan Sui at the South China Sea Institute of Oceanology, Chinese Academy of Sciences. Thanks for the 1971 nautical chart provided by Qinghua Gong and the 2012 nautical chart provided by Xia Wang. The GEBCO data can be downloaded from https://www.gebco.net/. The initial temperature and salinity data in the model are extracted from the World Ocean Atlas (2009, https://climatedataguide.ucar.edu/climate-data/world-ocean-atlas-woa09). The TPXO data can be downloaded from http://volkov.oce.orst.edu/tides/tpxo8_atlas.html. The NCEP reanalysis data are from https://www.psl.noaa.gov/data/reanalysis/reanalysis.shtml.

References

Booij N, Ris R C, Holthuijsen L H. 1999. A third-generation wave model for coastal regions: 1. Model description and validation. Journal of Geophysical Research, 104(C4): 7649–7666, doi: 10.1029/98JC02622

Burchard H, Schuttelaars H M, Ralston D K. 2018. Sediment trapping in estuaries. Annual Review of Marine Science, 10: 371–395, doi: 10.1146/annurev-marine-010816-060535

Chapman D C. 1985. Numerical treatment of cross-shelf open boundaries in a barotropic coastal ocean model. Journal of Physical Oceanography, 15(8): 1060–1075, doi: 10.1175/1520-0485(1985)015<1060:NTOCSO>2.0.CO;2

Chen Yongqin David, Chen Xiaohong. 2008. Modeling transport and

distribution of suspended sediments in Pearl River estuary. Journal of Coastal Research, (10052): 163–170, doi: 10.2112/1551-5036-52.sp1.163

Cloern J E. 1987. Turbidity as a control on phytoplankton biomass and productivity in estuaries. Continental Shelf Research, 7(11–12): 1367–1381, doi: 10.1016/0278-4343(87)90042-2

Dai Zhijun, Fagherazzi S, Mei Xuefei, et al. 2016. Linking the infilling of the north branch in the Changjiang (Yangtze) estuary to anthropogenic activities from 1958 to 2013. Marine Geology, 379: 1–12, doi: 10.1016/j.margeo.2016.05.006

Dai Zhijun, Liu J T, Fu Gui, et al. 2013. A thirteen-year record of bathymetric changes in the north passage, Changjiang (Yangtze) estuary. Geomorphology, 187: 101–107, doi: 10.1016/j.geomorph.2013.01.004

Dai Zhijun, Mei Xuefei, Darby S E, et al. 2018. Fluvial sediment transfer in the Changjiang (Yangtze) river-estuary depositional system. Journal of Hydrology, 566: 719–734, doi: 10.1016/j.jhydrol.2018.09.019

Dai S B, Yang S L, Cai A M. 2008. Impacts of dams on the sediment flux of the Pearl River, southern China. CATENA, 76(1): 36–43, doi: 10.1016/j.catena.2008.08.004

de Jonge V N, Schuttelaars H M, van Beusekom J E E, et al. 2014. The influence of channel deepening on estuarine turbidity levels and dynamics, as exemplified by the Ems estuary. Estuarine, Coastal and Shelf Science, 139: 46–59, doi: 10.1016/j.ecss.2013.12.030

Dijkstra Y M, Schuttelaars H M, Schramkowski G, et al. 2019. Modeling the transition to high sediment concentrations as a response to channel deepening in the Ems River Estuary. Journal of Geophysical Research, 124(3): 1578–1594, doi: 10.1029/2018JC014367

Dyer K R. 1974. The salt balance in stratified estuaries. Estuarine and Coastal Marine Science, 2(3): 273–281, doi: 10.1016/0302-3524(74)90017-6

Egbert G D, Erofeeva S Y. 2002. Efficient inverse modeling of Barotropic Ocean tides. Journal of Atmospheric and Oceanic Technology, 19(2): 183–204, doi: 10.1175/1520-0426(2002)019<0183:EIMOBO>2.0.CO;2

Flather R A. 1976. A tidal model of the Northwest European continental shelf. Memoires de la Societe Royale des Sciences de Liege, 6(10): 141–164

Haidvogel D B, Arango H, Budgell W P, et al. 2008. Ocean forecasting in terrain-following coordinates: formulation and skill assessment of the Regional Ocean Modeling System. Journal of Computational Physics, 227(7): 3595–3624, doi: 10.1016/j.jcp.2007.06.016

Hu Jiatang, Li Shiyu, Geng Bingxu. 2011. Modeling the mass flux budgets of water and suspended sediments for the river network and estuary in the Pearl River Delta, China. Journal of Marine Systems, 88(2): 252–266, doi: 10.1016/j.jmarsys.2011.05.002

Kalnay E, Kanamitsu M, Kistler R, et al. 1996. The NCEP/NCAR 40-year reanalysis project. Bulletin of the American Meteorological Society, 77(3): 437–472, doi: 10.1175/1520-0477(1996)077<0437:TNYRP>2.0.CO;2

Kerner M. 2007. Effects of deepening the Elbe Estuary on sediment regime and water quality. Estuarine, Coastal and Shelf Science, 75(4): 492–500, doi: 10.1016/j.ecss.2007.05.033

Lesourd S, Lesueur P, Brun-Cottan J C, et al. 2001. Morphosedimentary evolution of the macrotidal Seine estuary subjected to human impact. Estuaries, 24(6): 940, doi: 10.2307/1353008

Lin Shicheng, Liu Guangping, Niu Jianwei, et al. 2021. Responses of hydrodynamics to changes in shoreline and bathymetry in the Pearl River Estuary, China. Continental Shelf Research, 229: 104556, doi: 10.1016/j.csr.2021.104556

Liu Guangping, Cai Shuqun. 2019. Modeling of suspended sediment by coupled wave-current model in the Zhujiang (Pearl) River Estuary. Acta Oceanologica Sinica, 38(7): 22–35, doi: 10.1007/s13131-019-1455-3

Liu Feng, Hu Shuai, Guo Xiaojuan, et al. 2018. Recent changes in the sediment regime of the Pearl River (South China): causes and implications for the Pearl River Delta. Hydrological Processes, 32(12): 1771–1785, doi: 10.1002/hyp.11513

Liu Jintao, Hu Jiatang, Li Shiyu, et al. 2020. A model study on the short-term impact of reclamation on the hydrodynamic processes in the Lingdingyang Bay. Marine Science Bulletin, 39(02): 178–190, doi: 10.11840/j.issn.1001-6392.2020.02.005

Liu Yonggang, MaCready P, Hickey B M, et al. 2009. Evaluation of a coastal ocean circulation model for the Columbia River plume in summer 2004. Journal of Geophysical Research, 114(C2): C00B04, doi: 10.1029/2008JC004929

Luo Xianlin, Yang Qingshu, Jia Liangwen, et al. 2002. River-bed Evolution of the Pearl River Delta (in Chinese). Guangzhou: Sun Yat-sen University Press, 91–206

Meade R H. 1969. Landward transport of bottom sediments in estuaries of the Atlantic coastal plain. Journal of Sedimentary Research, 39(1): 222–234, doi: 10.1306/74D71C1C-2B21-11D7-8648000102C1865D

Mellor G L, Yamada T. 1982. Development of a turbulence closure model for geophysical fluid problems. Reviews of Geophysics, 20(4): 851–875, doi: 10.1029/RG020i004p00851

Orlanski I. 1976. A simple boundary condition for unbounded hyperbolic flows. Journal of Computational Physics, 21(3): 251–269, doi: 10.1016/0021-9991(76)90023-1

Shchepetkin A F, McWilliams J C. 2005. The regional oceanic modeling system (ROMS): a split-explicit, free-surface, topography-following-coordinate oceanic model. Ocean Modelling, 9(4): 347–404, doi: 10.1016/j.ocemod.2004.08.002

Shen Huanting, He Songling, Mao Zhichang, et al. 2001. On the turbidity maximum in the Chinese estuaries. Journal of Sediment Research (in Chinese), (1): 23–29, doi: 10.3321/j.issn:0468-155X.2001.01.004

Song Yuhe, Haidvogel D. 1994. A semi-implicit ocean circulation model using a generalized topography-following coordinate system. Journal of Computational Physics, 115(1): 228–244, doi: 10.1006/jcph.1994.1189

Styles R, Glenn S M. 2000. Modeling stratified wave and current bottom boundary layers on the continental shelf. Journal of Geophysical Research, 105(10): 24119–24139, doi: 10.1029/2000JC900115

Tan Chao, Huang Bensheng, Liu Kunsong, et al. 2017. Using the wavelet transform to detect temporal variations in hydrological processes in the Pearl River, China. Quaternary International, 440: 52–63, doi: 10.1016/j.quaint.2016.02.043

van der Wal D, Pye K, Neal A. 2002. Long-term morphological change in the Ribble Estuary, northwest England. Marine Geology, 189(3/4): 249–266, doi: 10.1016/S0025-3227(02)00476-0

van Maren D S, van Kessel T, Cronin K, et al. 2015. The impact of channel deepening and dredging on estuarine sediment concentration. Continental Shelf Research, 95: 1–14, doi: 10.1016/j.csr.2014.12.010

Wai O W H, Wang C H, Li Y S, et al. 2004. The formation mechanisms of turbidity maximum in the Pearl River Estuary, China. Marine Pollution Bulletin, 48(5–6): 441–448, doi: 10.1016/j.marpolbul.2003.08.019

Warner J C, Sherwood C R, Signell R P, et al. 2008. Development of a three-dimensional, regional, coupled wave, current, and sediment-transport model. Computers & Geosciences, 34(10): 1284–1306, doi: 10.1016/j.cageo.2008.02.012

Willmott C J. 1981. On the validation of models. Physical Geography, 2(2): 184–194, doi: 10.1080/02723646.1981.10642213

Wei Xing, Cai Shuqun, Zhan Weikang, et al. 2021. Changes in the distribution of surface sediment in Pearl River Estuary, 1975–2017, largely due to human activity. Continental Shelf Research, 228, doi: 10.1016/j.csr.2021.104538

Wu Z Y, Saito Y, Zhao D N, et al. 2016. Impact of human activities on subaqueous topographic change in Lingding Bay of the Pearl River estuary, China, during 1955–2013. Scientific Reports, 6: 37742, doi: 10.1038/srep37742

Xie Lili, Liu Xia, Yang Qingshu, et al. 2015. Variations of current and sediment transport in Lingding Bay during spring tide in flood season driven by human activities. Journal of Sediment Re-

search (in Chinese), (3): 56–62, doi: 10.16239/j.cnki.0468-155x.2015.03.009

Yan Dong, Song Dehai, Bao Xianwen. 2020. Spring-neap tidal variation and mechanism analysis of the maximum turbidity in the Pearl River Estuary during flood season. Journal of Tropical Oceanography (in Chinese), 39(1): 20–35

Yang Liuzhu, Liu Feng, Gong Wenping, et al. 2019. Morphological response of Lingding Bay in the Pearl River Estuary to human intervention in recent decades. Ocean & Coastal Management, 176: 1–10, doi: 10.1016/j.ocecoaman.2019.04.011

Yao Zhangmin, Wang Yongyong, Li Aiming. 2009. Primary analysis of water distribution ratio variation in main waterway in Pearl River Delta. Pearl River (in Chinese), (2): 43–45, 51

Zeng Xiangming, He Ruoying, Xue Zuo, et al. 2015. River-derived sediment suspension and transport in the Bohai, Yellow, and East China Seas: a preliminary modeling study. Continental Shelf Research, 111: 112–125, doi: 10.1016/j.csr.2015.08.015

Zhan Weikang, Wu Jie, Wei Xing, et al. 2019. Spatio-temporal variation of the suspended sediment concentration in the Pearl River Estuary observed by MODIS during 2003–2015. Continental Shelf Research, 172: 22–32, doi: 10.1016/j.csr.2018.11.007

Zhang Guang, Chen Yuren, Cheng Weicong, et al. 2021a. Wave effects on sediment transport and entrapment in a channel-shoal estuary: the Pearl River Estuary in the dry winter season. Journal of Geophysical Research, 126(4): e2020JC016905, doi: 10.1029/2020JC016905

Zhang Guang, Cheng Weicong, Chen Lianghong, et al. 2019. Transport of riverine sediment from different outlets in the Pearl River Estuary during the wet season. Marine Geology, 415: 105957, doi: 10.1016/j.margeo.2019.06.002

Zhang Ping, Yang Qingshu, Wang Heng, et al. 2021b. Stepwise alterations in tidal hydrodynamics in a highly human-modified estuary: the roles of channel deepening and narrowing. Journal of Hydrology, 597: 126153, doi: 10.1016/j.jhydrol.2021.126153